

# Observational studies on S-bearing molecules in massive star forming regions

R. Luo<sup>1</sup>, J. Z. Wang<sup>1</sup>, X. Zhang<sup>2</sup>, D. H. Quan<sup>3</sup>, X. J. Jiang<sup>3</sup>, J. Li<sup>4</sup>, Q. Gou<sup>5</sup>, Y.Q. Li<sup>4</sup>, Y.N. Xu<sup>1</sup>, S.Q. Zheng<sup>4</sup>, C. Ou<sup>1</sup>, and Y.J. Liu<sup>6</sup>

<sup>1</sup> Guangxi Key Laboratory for Relativistic Astrophysics, School of Physical Science and Technology, Guangxi University, Nanning 530004, PR China

e-mail: junzhiwang@gxu.edu.cn

<sup>2</sup> Xinjiang Astronomical Observatory, Chinese Academy of Sciences, 150 Science 1-Street, Urumqi, Xinjiang 830011, PR China

<sup>3</sup> Research Center for Intelligent Computing Platforms, Zhejiang Laboratory, Hangzhou, 311100, PR China

<sup>4</sup> Shanghai Astronomical Observatory, Chinese Academy of Sciences No. 80 Nandan Road Shanghai, 200030, PR China

<sup>5</sup> School of Chemistry and Chemical Engineering, Chongqing University, Daxuecheng South Road. 55, Chongqing 401331, PR China

<sup>6</sup> Department of Physics, Anhui Normal University, Wuhu, Anhui 241002, PR China

Received xx; accepted xxx

## ABSTRACT

*Context.* S-bearing molecules are powerful tools for physical conditions inside massive star forming region. The abundances of S-bearing molecules, including H<sub>2</sub>S, H<sub>2</sub>CS, and HCS<sup>+</sup>, are highly dependent on physical and chemical changes, which means that they are good tracers of the evolutionary stage of massive star formation.

*Aims.* We present observational results of H<sub>2</sub>S 1<sub>10-101</sub>, H<sub>2</sub><sup>34</sup>S 1<sub>10-101</sub>, H<sub>2</sub>CS 5<sub>14-414</sub>, HCS<sup>+</sup> 4-3, SiO 4-3, HC<sub>3</sub>N 19-18 and C<sup>18</sup>O 1-0 toward a sample of 51 late-stage massive star-forming regions, to study relationships among H<sub>2</sub>S, H<sub>2</sub>CS, HCS<sup>+</sup> and SiO in hot cores. Chemical connections of these S-bearing molecules are discussed based on the relations between relative abundances in sources.

*Methods.* H<sub>2</sub><sup>34</sup>S 1<sub>10-101</sub>, as the isotopic line of H<sub>2</sub>S 1<sub>10-101</sub>, was used to correct optical depths of H<sub>2</sub>S 1<sub>10-101</sub>. Beam averaged column densities of all molecules were calculated, as well as relative abundances of H<sub>2</sub>S, H<sub>2</sub>CS, and HCS<sup>+</sup> to that of H<sub>2</sub>, which were derived from C<sup>18</sup>O. One chemical model including gas, dust grain surface and icy mantle phases, for H<sub>2</sub>S, H<sub>2</sub>CS, and HCS<sup>+</sup> molecules, was used to compare with the observed abundances.

*Results.* H<sub>2</sub>S 1<sub>10-101</sub>, H<sub>2</sub><sup>34</sup>S 1<sub>10-101</sub>, H<sub>2</sub>CS 5<sub>14-414</sub>, HCS<sup>+</sup> 4-3 and HC<sub>3</sub>N 19-18 were detected in 50 of the 51 sources, while SiO 4-3 was detected in 46 sources. C<sup>18</sup>O 1-0 was detected in all sources. The Pearson correlation coefficients between H<sub>2</sub>CS and HCS<sup>+</sup> normalized by H<sub>2</sub> and H<sub>2</sub>S are 0.94 and 0.87, respectively, and a tight linear relationship is found between them with slope of 1.00 and 1.09, while they are 0.77 and 0.98 between H<sub>2</sub>S and H<sub>2</sub>CS, respectively, and 0.76 and 0.97 between H<sub>2</sub>S and HCS<sup>+</sup>. The values of full width at half maxima (FWHM) of H<sub>2</sub><sup>34</sup>S 1<sub>10-101</sub>, H<sub>2</sub>CS 5<sub>14-414</sub>, HCS<sup>+</sup> 4-3, and HC<sub>3</sub>N 19-18 in each source are similar to each other, which indicate that they can trace similar regions. Comparing the observed abundance with model results, there is one possible time (2-3×10<sup>5</sup> yr) for each source in the model that match the measured abundances of H<sub>2</sub>S, H<sub>2</sub>CS and HCS<sup>+</sup>. The abundances of HCS<sup>+</sup>, H<sub>2</sub>CS, and H<sub>2</sub>S increase with the increment of SiO abundance in these sources, which implies that shock chemistry may be important for them.

*Conclusions.* Close abundance relation of H<sub>2</sub>S, H<sub>2</sub>CS and HCS<sup>+</sup> molecules and similar line widths in observational results indicate that these three molecules could be chemically linked, with HCS<sup>+</sup> and H<sub>2</sub>CS the most correlated. The comparison of the observational results with chemical models shows that the abundances can be reproduced for almost all the sources at a specific time. The observational results, including abundances in these sources need to be considered in further modeling H<sub>2</sub>S, H<sub>2</sub>CS and HCS<sup>+</sup> in hot cores with shock chemistry.

**Key words.** ISM: clouds – ISM: molecules – ISM: abundances

## 1. Introduction

As the 10th most abundant element in the universe with relative abundance to hydrogen of  $\sim 1.3 \times 10^{-5}$  (Asplund et al. 2005), sulfur (S) was found in many molecules, which is important for understanding gas chemistry in molecular clouds with different phases. There are more than a dozen S-bearing molecules that were detected in interstellar molecular clouds and/or outflows, including SH, SH<sup>+</sup>, SO, SO<sub>2</sub>, CS, C<sub>2</sub>S, C<sub>3</sub>S, CH<sub>3</sub>SH, NS, SiS, H<sub>2</sub>S, H<sub>2</sub>CS, HCS<sup>+</sup>, OCS, HNCS, and HSCN (Gottlieb et al. 1978; Frerking et al. 1979; Brown et al. 1980; Blake et al. 1987; Drdla et al. 1989; Turner 1989; Adande et al. 2010; Esplugues et al. 2013; Neufeld et al. 2015; Li et al. 2015; Luo et

al. 2019; Cernicharo et al. 2000). Even though S abundance in diffuse HI medium is still consistent with cosmic value (Jenkins 2009), the main reservoir of S in dense clouds and hot core is still unclear (Vidal & Wakelam 2018), since the derived abundance of dense clouds only account for  $\sim 0.01$  of the cosmic abundance of atomic S (Charnley 1997).

S-bearing molecules are thought to be useful tracers of chemical and physical properties of complex star forming regions (SFRs) located in dense molecular clouds and can be used to study the evolutionary stages of massive star formation (Esplugues et al. 2014). Esplugues et al. (2013) showed that S-bearing molecules exhibit higher column densities, up to three

orders of magnitude, in the high-velocity plateau of Orion KL affected by shocks, with respect to quiet regions of the clouds. Therefore, they are also considered to be good tracers for shocks. S-bearing molecules, released from ice mantles at  $T \sim 100\text{--}300$  K, such as SO, H<sub>2</sub>S, H<sub>2</sub>CS, OCS, can probe hot cores in low-mass protostellar Class 0 system (Tychoniec et al. 2021). Fontani et al. (2023) find for a sample of massive star-forming regions that NS, CCS, and HCS<sup>+</sup> trace cold, quiescent, and likely extended material, while OCS and SO<sub>2</sub> trace warmer, more turbulent, and likely denser and more compact material. On the other hand, SO traces both quiescent and turbulent material. But the chemical origin of H<sub>2</sub>S and H<sub>2</sub>CS is less clear.

Sulfur and oxygen are part of the chalcogens group in the periodic table, with similar electronic structure and chemical bond, meaning that they usually have a similar reactivity in chemical reactions (Miessler et al. 2013). As the third most abundant element after hydrogen and helium in the interstellar medium (ISM), oxygen cosmic abundance is of  $O/H \sim 2.5 \times 10^{-4}$  (Lis et al. 2023). H<sub>2</sub>O, H<sub>2</sub>CO and HCO<sup>+</sup>, listed in order of decreasing abundances in the ISM, are important oxygen-containing molecules with close astrochemical relationships. Replacing O by S, H<sub>2</sub>S, H<sub>2</sub>CS and HCS<sup>+</sup> molecules should play important roles for understanding chemical network of S-bearing molecules in ISM, with relative high abundances among S-bearing molecules. For example, the abundances of H<sub>2</sub>S, H<sub>2</sub>CS and HCS<sup>+</sup> molecules normalized by H<sub>2</sub> are  $4.6 \times 10^{-8}$ ,  $1.3 \times 10^{-9}$  and  $1.5 \times 10^{-10}$ , respectively, in G328.2551-0.5321 (Bouscasse et al. 2022).

There are few observational studies for H<sub>2</sub>S, H<sub>2</sub>CS, and HCS<sup>+</sup> molecules toward hot cores (Esplugues et al. 2013; Li et al. 2015; Kalenskii et al. 2022; el Akel et al. 2022; Esplugues et al. 2023). The dominant S-bearing species in ices are still in debate. H<sub>2</sub>S was suggested as one, since predicted to be to abundant on the grain surface in low gas and dust temperature environment (Vidal et al. 2017; Navarro-Almáida et al. 2020, <20 K), but it has not still been detected on ices (McClure et al. 2023). Once H<sub>2</sub>S molecules formed, they rapidly initiate reactions that drive the production of other S-bearing molecules (Druard & Wakelam 2012). The formation of S-bearing molecules is closely related to the environment, i.e. temperature (Druard & Wakelam 2012), UV photons and high energy protons (Jiménez-Escobar & Muñoz Caro 2011), ion irradiation (Garozzo et al. 2010). In molecular clouds, ion-molecular reactions are most important (Goldsmith & Linke 1980), while in warm gases of hot cores and shock waves, neutral-neutral reactions mainly occur (Charnley 1997). H<sub>2</sub>CS may be formed by CH + H<sub>2</sub>S in the gas phase of massive star forming regions such as Orion KL and Sgr B2 as predicted by a astrochemical model (Inostroza-Pino et al. 2020). What's more, H<sub>2</sub>CS can be formed via S + CH<sub>3</sub> and destroyed with C<sup>+</sup> in gas-phase (Esplugues et al. 2022). Finally, HCS<sup>+</sup> may be formed by CS + H<sub>3</sub><sup>+</sup> and CS<sup>+</sup> + H<sub>2</sub> in high-mass star forming cores. (Shingledecker et al. 2020; Fontani et al. 2023) The dissociative recombination rate of HCS<sup>+</sup> is substantially larger than those of other isoelectronic ions, which had substantial effect on the abundances of molecules and ions in the low-temperature environment of interstellar clouds (Montaigne et al. 2005). However, there are still lack of sufficient studies, including H<sub>2</sub>S, H<sub>2</sub>CS, HCS<sup>+</sup> detections and the relationship among the three molecules in massive star forming regions.

In this paper, we present H<sub>2</sub>S 1<sub>10</sub>-1<sub>01</sub>, H<sub>2</sub><sup>34</sup>S 1<sub>10</sub>-1<sub>01</sub>, H<sub>2</sub>CS 5<sub>14</sub>-4<sub>14</sub>, HCS<sup>+</sup> 4-3, SiO 4-3, HC<sub>3</sub>N 19-18 and C<sup>18</sup>O 1-0 single pointing observations toward a sample of 51 massive star forming regions using the Institut de Radioastronomie Millimétrique

(IRAM) 30-m telescope. The observations are described in Section 2, while the results are reported in Section 3. Discussions are presented in Section 4, and a brief summary is in Section 5.

## 2. Observations and analysis

### 2.1. Observations and data reduction

The sample, which is selected from Reid et al. (2014, 2019) with measurements of trigonometric parallaxes, includes 51 late-stage massive star-forming regions with 6.7 GHz methanol masers. The observations were taken with Institut de Radioastronomie Millimétrique (IRAM) 30-m millimeter telescope at Pico Veleta Spain during 2016 June and October, 2017 August, and 2020 August. The 3-mm (E0) and 2-mm (E1) bands of the Eight Mixer Receiver (EMIR) were used simultaneously with the Fourier Transform Spectrometers (FTS) backend to cover  $8 \times 4$  GHz bandwidth and 195 kHz spectral resolution for each band with dual polarization. More information can be found in Li et al. (2022). The spectral lines, H<sub>2</sub>S 1<sub>10</sub>-1<sub>01</sub> at 168762.7623MHz, H<sub>2</sub><sup>34</sup>S 1<sub>10</sub>-1<sub>01</sub> at 167910.516MHz, H<sub>2</sub>CS 5<sub>14</sub>-4<sub>14</sub> at 169114.160MHz, HCS<sup>+</sup> 4-3 at 170691.603MHz, HC<sub>3</sub>N 19-18 at 172849.287MHz, SiO 4-3 at 173688.274MHz, and C<sup>18</sup>O 1-0 at 109782.1734MHz, were included in the observations and used for scientific analyses in this paper. Table 1 shows the source names, aliases, equatorial coordinates and galactocentric distance in columns 1-4. The spectroscopic information parameters of H<sub>2</sub>S, H<sub>2</sub><sup>34</sup>S, H<sub>2</sub>CS, HCS<sup>+</sup>, SiO, HC<sub>3</sub>N and C<sup>18</sup>O lines are presented in Table 2.

The beam size of IRAM 30-m telescope is 22.4'' at 110 GHz and 14.3'' at 172 GHz. The main beam brightness temperature ( $T_{mb}$ ) is obtained by  $T_{mb} = T_A^* \cdot F_{eff} / B_{eff}$ , where  $T_A^*$  is antenna temperature, while  $F_{eff}$  is forward efficiency and  $B_{eff}$  is main beam efficiency.  $F_{eff}$  and  $B_{eff}$  are 94% and 78% in 3-mm band at 110 GHz, respectively, while they are 93% and 73%, respectively, in 2-mm band at 173 GHz.

The data was proceeded with CLASS package in GILDAS software<sup>1</sup>. After averaging the spectra for each sources to one single spectrum at 2mm and 3mm band respectively, the lines were identified and first-order baseline was removed. The velocity integrated flux, peak intensity, central velocity of each line were derived for most of the lines with single component Gaussian fitting. Otherwise, "print area" in CLASS was used to derive velocity integrated flux if the line profile can not be well fitted with single component Gaussian fitting (see Figure 1), which are caused by self-absorption and/or multiple components (see Figure 1b and 1c), for lines above  $3\sigma$  level, while H<sub>2</sub><sup>34</sup>S 1<sub>10</sub>-1<sub>01</sub> was used to determine the velocity range of each source.

### 2.2. Methods

An optically thin transition produces an antenna temperature that is proportional to the column density in the upper level of the transition being observed (Goldsmith & Langer 1999). However, since sulfur is the 10th most abundant element in the universe and H<sub>2</sub>S is likely the dominant molecular form of the S element in molecular clouds, H<sub>2</sub>S lines are usually optically thick. Some of the H<sub>2</sub>S 1<sub>10</sub>-1<sub>01</sub> lines showed a pit around line center on the spectrum level, as the signature of self-absorption. Since H<sub>2</sub><sup>34</sup>S 1<sub>10</sub>-1<sub>01</sub> lines were also detected with H<sub>2</sub>S 1<sub>10</sub>-1<sub>01</sub> detection, we use the beam averaged column densities of H<sub>2</sub><sup>34</sup>S to calculate

<sup>1</sup> <http://www.iram.fr/IRAMFR/GILDAS>

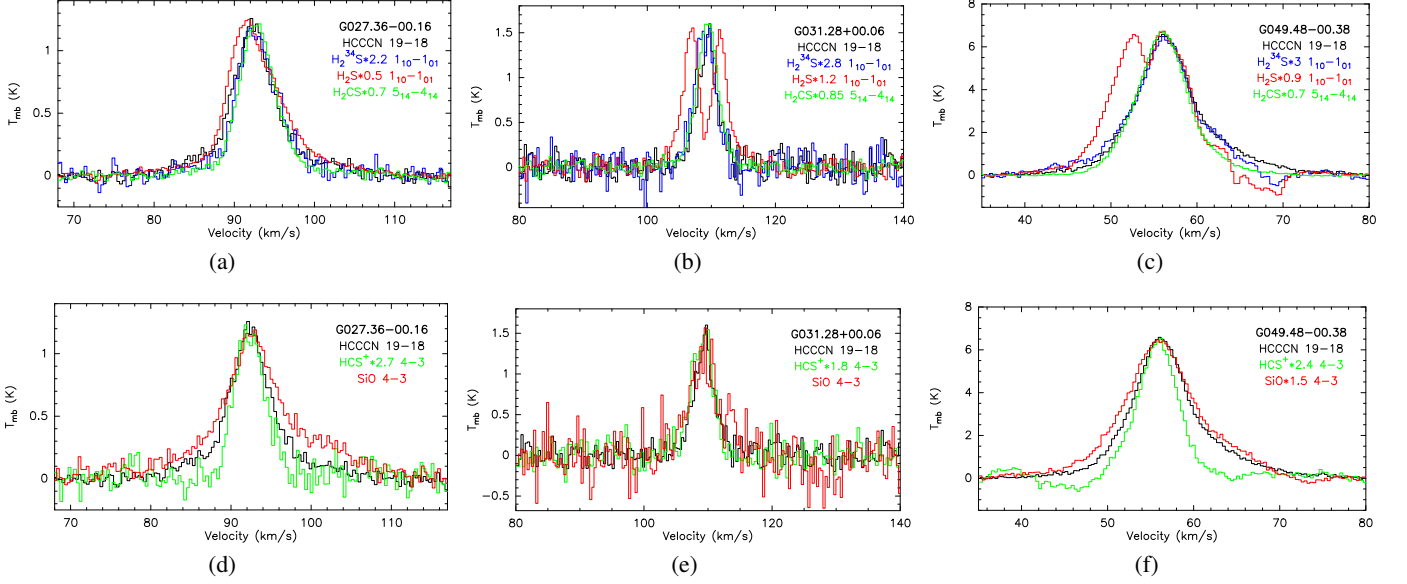


Fig. 1: The spectra of  $\text{H}_2\text{S}$   $1_{10}-1_{01}$ ,  $\text{H}_2^{34}\text{S}$   $1_{10}-1_{01}$ ,  $\text{H}_2\text{CS}$   $5_{14}-4_{14}$  detected with IRAM 30-m for three sources are shown in (a), (b) and (c), while  $\text{HCS}^+$  4-3,  $\text{SiO}$  4-3 lines are shown in (d), (e) and (f). All of the observed spectra are aligned to the peak with  $\text{HC}_3\text{N}$  19-18. In (a), (b) and (c), red lines are  $\text{H}_2\text{S}$   $1_{10}-1_{01}$ , blue lines are  $\text{H}_2^{34}\text{S}$   $1_{10}-1_{01}$ , green lines are  $\text{H}_2\text{CS}$   $5_{14}-4_{14}$ . In (d), (e) and (f),  $\text{HCS}^+$  4-3 lines are marked in green, while  $\text{SiO}$  4-3 lines are red. The black lines in all figure are  $\text{HC}_3\text{N}$

those of  $\text{H}_2\text{S}$ , by  $^{32}\text{S}/^{34}\text{S}$  ratio, as function of galactocentric distance, which was from Yan et al. (2023) given by

$$^{32}\text{S}/^{34}\text{S} = (0.75 \pm 0.13)R_{GC} + (15.52 \pm 0.78) \quad (1)$$

The beam-averaged column density is given by:

$$N_{tot} = \frac{8\pi k\nu^2}{hc^3 A_{ul}} \frac{Q(T_{ex})}{g_u} e^{\frac{E_u}{kT_{ex}}} \int T_{mb} dv \quad (\text{cm}^{-2}) \quad (2)$$

For above function,  $k$  is the Boltzmann constant,  $\nu$  is the transition frequency,  $h$  is the Planck constant,  $c$  is the speed of light,  $A_{ul}$  is the Einstein emission coefficient,  $g_u$  is upper state degeneracy and  $E_u$  is upper state energy. For sources with non-detection,  $3\sigma$  upper limits for the integrated intensity,  $\int T_{mb} dv$ , were calculated with  $3 \times rms \sqrt{\delta\nu\Delta\nu}$ , where  $\delta\nu$  is the channel separation in velocity,  $rms$  is the root mean square for line free channel from first-order linear fitting using the remaining channels, which are masked the signal area, and  $\Delta\nu$  is the line width.

After assuming unity beam filling factor, and local thermodynamic equilibrium (LTE) approximation for all molecules with the same excitation temperature ( $T_{ex}$ ) of 18.75 K for  $\text{H}_2^{34}\text{S}$ ,  $\text{H}_2\text{CS}$ ,  $\text{HCS}^+$ ,  $\text{SiO}$ , and  $\text{C}^{18}\text{O}$ , as well as optically thin for the lines of all these molecules, the beam averaged column densities were calculated. Since the  $\text{H}_2^{34}\text{S}$ ,  $\text{H}_2\text{CS}$ ,  $\text{HCS}^+$  molecules are normally sub-thermal in these sources, the used  $T_{ex}$  of these spectral lines are lower than kinetic temperature ( $T_k$ ). The partition function ( $Q(T_{ex})$ ) for each molecule was obtained at  $T_{ex}=18.75$  K, checked by Radex on line calculator (van der Tak et al. 2007). For example, the upper level population of  $\text{H}_2^{34}\text{S}$   $1_{10}-1_{01}$  over all energy levels (POP-UP) are obtained by RADEX. When  $T_k$  ranges from 30 K to 150 K and density of  $\text{H}_2$  is  $1 \times 10^5 \text{ cm}^{-3}$ , POP-UP increases from 0.163 to

0.267.  $Q(T_{ex})$  were obtained from Cologne Database for Molecular Spectroscopy (CDMS)<sup>2</sup> (Müller et al. 2001, 2005). Under LTE approximation with  $T_{ex} = 18.75$  K,  $g_u e^{\frac{E_u}{kT_{ex}}} / Q(T_{ex})$ , which is the same parameter as POP-UP in the results of RADEX for calculating total column density, is equal to 0.234. We also calculated the systemic bias of estimating column densities with excitation temperature of 37.5 K (0.177), 25 K (0.222) and 10 K (0.150), which is about 1.32, 1.05 and 1.55 times, respectively, of that with  $T_{ex} = 18.75$  K for  $\text{H}_2^{34}\text{S}$  molecules. The column densities of  $\text{H}_2$  can be derived with  $\text{C}^{18}\text{O}$  by  $N_{\text{H}_2} = 4.37 \times 10^6 N_{\text{C}^{18}\text{O}}$  (Frerking et al. 1982).

In addition to using  $\text{H}_2^{34}\text{S}$  column densities with the ratio of  $^{32}\text{S}/^{34}\text{S}$  to directly calculate the column density of  $\text{H}_2\text{S}$ , there is another method that correcting the optical depths of  $\text{H}_2\text{S}$  to get the column density. Assuming  $\text{H}_2\text{S}$  and  $\text{H}_2^{34}\text{S}$   $1_{10}-1_{01}$  lines in each source have the same excitation temperature ( $T_{ex}$ ) and molecular abundance ratio is approximately equal to isotopic abundance ratio as  $\frac{^{32}\text{S}}{^{34}\text{S}} = \frac{\text{H}_2^{32}\text{S}}{\text{H}_2^{34}\text{S}}$  (hear-after  $\text{H}_2\text{S}$  for  $\text{H}_2^{32}\text{S}$ ). Then,  $\tau_{\text{H}_2\text{S}}$  is calculated by

$$\frac{1 - e^{-\tau_{\text{H}_2\text{S}}}}{1 - e^{-\tau_{\text{H}_2^{34}\text{S}}}} = \frac{\int T_{mb}(\text{H}_2\text{S}) dv}{\int T_{mb}(\text{H}_2^{34}\text{S}) dv} \quad (3)$$

The range of calculated  $\tau_{\text{H}_2\text{S}}$  is from 0.53 in G232.62+00.99 to 11.2 in G010.47+00.02 (see Table A.1). The calculation formula of column density is slightly different from that of Eq.(1), which given by

$$N_{tot} = \frac{8\pi k\nu^2}{hc^3 A_{ul}} \frac{Q(T_{ex})}{g_u} e^{\frac{E_u}{kT_{ex}}} \frac{\tau}{1 - e^{-\tau}} \int T_{mb} dv \quad (\text{cm}^{-2}) \quad (4)$$

<sup>2</sup> [https://cdms.astro.uni-koeln.de/classic/predictions/catalog/partition\\_function.html](https://cdms.astro.uni-koeln.de/classic/predictions/catalog/partition_function.html)

Comparing the column densities obtained by the two methods, we found that the column densities directly from  $\text{H}_2^{34}\text{S}$  using the  $^{32}\text{S}/^{34}\text{S}$  ratio were lower than that from optical depth of the  $\text{H}_2\text{S}$  transition, with 0.85 times in columns 1-2 of Table B.1.

### 3. Results

#### 3.1. The detected lines

$\text{H}_2\text{S}$   $1_{10-1_{01}}$ ,  $\text{H}_2^{34}\text{S}$   $1_{10-1_{01}}$ ,  $\text{H}_2\text{CS}$   $5_{14-4_{14}}$ ,  $\text{HCS}^+$  4-3 and  $\text{HC}_3\text{N}$  19-18 were detected in all sources except for G012.90-00.24, while  $\text{SiO}$  4-3 was detected in 46 sources.  $\text{C}^{18}\text{O}$  1-0 was detected in all sources (see Figure 1 and A.1).  $\text{H}_2\text{S}$   $1_{10-1_{01}}$  lines are normally stronger than  $\text{H}_2\text{CS}$   $5_{14-4_{14}}$ , while  $\text{H}_2\text{CS}$   $5_{14-4_{14}}$  are stronger than  $\text{HCS}^+$  4-3. The sources can be divided into three groups based in the line profile of  $\text{H}_2\text{S}$   $1_{10-1_{01}}$  and  $\text{H}_2^{34}\text{S}$   $1_{10-1_{01}}$ . In 26 sources of the sample both lines can be fitted with a single Gaussian component, such as G027.36-00.16 (see Figure 1a), while in 21 sources,  $\text{H}_2\text{S}$   $1_{10-1_{01}}$  needs from two to four components, and this is probably caused by inflowing gas, such as G031.28+00.06 (see Figure 1b). There are three sources, G049.48-00.38 (W51M, see Figure 1c), G043.16+00.01 (W49N) and G000.67-00.03 (SgrB2), in which there is a possible optically thin velocity component of  $\text{H}_2\text{S}$   $1_{10-1_{01}}$  without corresponding  $\text{H}_2^{34}\text{S}$   $1_{10-1_{01}}$  emission. The column densities of  $\text{H}_2\text{S}$  have been calculated by those of  $\text{H}_2^{34}\text{S}$  for all the sources.

$\text{HC}_3\text{N}$  19-18 was used to confirm the central velocities and line profile of S-bearing lines, while  $\text{C}^{18}\text{O}$  was used to get  $\text{H}_2$  column densities to obtain the relative  $\text{H}_2\text{S}$ ,  $\text{H}_2\text{CS}$ , and  $\text{HCS}^+$  abundances.  $\text{SiO}$  was used as the tracer of shock activities in star formation regions.

Table 1 show the molecular species, velocity-integrated intensities, central velocity, and peak temperature, which are listed in columns 5-8. Velocity integrated fluxes were obtained from the single component Gaussian fitting, or with “print area” for  $\text{H}_2\text{S}$ ,  $\text{H}_2\text{CS}$  and  $\text{C}^{18}\text{O}$  in CLASS if complex line profile was found as explained in Section 2.2, which was noted by “a” superscript in columns 4 of Table 1. As shown in Table 1, the velocity-integrated intensities and peak temperature of  $\text{H}_2\text{S}$   $1_{10-1_{01}}$  are higher than  $\text{H}_2\text{CS}$   $5_{14-4_{14}}$ , while  $\text{H}_2\text{CS}$   $5_{14-4_{14}}$  are higher than  $\text{HCS}^+$  4-3. The S-bearing species studied in this work present similar line width, while  $\text{SiO}$  4-3 presents broader line width than other lines in each source.

#### 3.2. Column densities

The beam averaged column densities of  $\text{H}_2\text{S}$ ,  $\text{H}_2^{34}\text{S}$ ,  $\text{H}_2\text{CS}$ ,  $\text{HCS}^+$ ,  $\text{SiO}$  and  $\text{C}^{18}\text{O}$  molecules are shown in Table B.1, with the range of  $\text{H}_2\text{S}$  from  $3.59 \times 10^{13}$  to  $3.50 \times 10^{15} \text{cm}^{-2}$ ,  $\text{H}_2^{34}\text{S}$  from  $1.65 \times 10^{12}$  to  $1.83 \times 10^{14} \text{cm}^{-2}$ ,  $\text{H}_2\text{CS}$  from  $7.09 \times 10^{12}$  to  $1.25 \times 10^{15} \text{cm}^{-2}$  and  $\text{HCS}^+$  from  $6.67 \times 10^{11}$  to  $6.04 \times 10^{13} \text{cm}^{-2}$ , as lowest abundant S-bearing molecules among  $\text{H}_2\text{S}$ ,  $\text{H}_2\text{CS}$  and  $\text{HCS}^+$ . The resulting column densities for  $\text{SiO}$  and  $\text{C}^{18}\text{O}$  molecules in these 50 sources were from  $3.33 \times 10^{11}$  to  $9.25 \times 10^{13} \text{cm}^{-2}$ , and from  $6.30 \times 10^{15}$  to  $3.76 \times 10^{16} \text{cm}^{-2}$ , respectively. The column densities of  $\text{H}_2$  are obtained by  $\text{C}^{18}\text{O}$  with  $N_{\text{H}_2} = 4.37 \times 10^6 N_{\text{C}^{18}\text{O}}$  (Frerking et al. 1982), ranging from  $1.13 \times 10^{22}$  to  $4.80 \times 10^{23} \text{cm}^{-2}$ .

#### 3.3. Relative abundances

Relative abundances of these molecules, which can be obtained with beam averaged column densities, are more important than

the beam averaged column densities themselves for scientific analyses. The abundances of  $\text{H}_2\text{S}$ ,  $\text{H}_2\text{CS}$  and  $\text{HCS}^+$  normalized by  $\text{H}_2$  were shown in column 4-6 of Table D.1, where  $\text{H}_2\text{S}$  are obtained from  $\text{H}_2^{34}\text{S}$  multiplied by the  $^{32}\text{S}/^{34}\text{S}$ . The relation between the abundances of  $\text{H}_2\text{S}$  and  $\text{HCS}^+$  normalized by  $\text{H}_2$  was presented in Figure 2a, with Pearson correlation coefficient<sup>3</sup> of 0.76, slope of 0.97, using least square fitting, while the Pearson correlation coefficients and slope between the abundances of  $\text{H}_2\text{S}$  and  $\text{H}_2\text{CS}$  normalized by  $\text{H}_2$  (see Figure 2b) were 0.77 and 0.98, respectively. For the abundances of  $\text{H}_2\text{CS}$  and  $\text{HCS}^+$  normalized  $\text{H}_2$  (see Figure 2c), the Pearson correlation coefficients and slope were 0.94 and 1.00. Since the slopes and Pearson correlation coefficients among them are positive numbers close or equal to 1,  $\text{H}_2\text{S}$ ,  $\text{H}_2\text{CS}$  and  $\text{HCS}^+$  molecules are probably very closely chemically related to each other.

The relative abundances of  $\text{H}_2\text{S}$ ,  $\text{H}_2\text{CS}$ , and  $\text{HCS}^+$  normalized by  $\text{H}_2$  span more than one order of magnitude in these 50 sources. Table E.1 showed the abundance ratio [ $\text{H}_2\text{S}/\text{H}_2\text{CS}$ ], [ $\text{H}_2\text{S}/\text{HCS}^+$ ], [ $\text{H}_2\text{CS}/\text{HCS}^+$ ] towards all the sources. The abundance ratio of [ $\text{H}_2\text{S}/\text{H}_2\text{CS}$ ] ranges from  $1.32 \pm 0.12$  in G000.67-00.03 to  $10.2 \pm 0.49$  in G109.87+02.11, with median value of 4.4, while it ranges from  $14.1 \pm 7.01$  in G011.49-01.48 to  $129.6 \pm 11.1$  in G109.87+02.11 with median value of 63.8 for [ $\text{H}_2\text{S}/\text{HCS}^+$ ] and from  $7.94 \pm 0.61$  in G232.62+00.99 to  $23.6 \pm 0.96$  in G049.48-00.36 with median value of 13.0 for [ $\text{H}_2\text{CS}/\text{HCS}^+$ ].

Good correlation can be found between  $\text{H}_2\text{CS}$  and  $\text{HCS}^+$  whether normalized by  $\text{H}_2\text{S}$  or  $\text{H}_2$ . (see Figure 3 and 2c). The abundance ratios of [ $\text{H}_2\text{CS}/\text{HCS}^+$ ] is well within a narrower ranges than that of [ $\text{H}_2\text{S}/\text{HCS}^+$ ] and [ $\text{H}_2\text{S}/\text{H}_2\text{CS}$ ] (see Table E.1). G011.49-01.48 and G0168.06+00.82, with large errors, are also marked in Figure 2 and 3, where  $\text{H}_2^{34}\text{S}$  lines showed weak emission.

The relationships between S-bearing molecules and  $\text{SiO}$ , normalized by  $\text{H}_2$ , are shown in Figure 4, with Pearson correlation coefficients of  $\text{HCS}^+$ ,  $\text{H}_2\text{CS}$ , and  $\text{H}_2\text{S}$  with  $\text{SiO}$  as 0.60, 0.68, 0.57, while slopes are 0.73, 0.75, 0.72, respectively. Even though the correlations are not as good as that of in between the S-bearing molecules themselves (see Figure 2), the abundances of  $\text{HCS}^+$ ,  $\text{H}_2\text{CS}$ , and  $\text{H}_2\text{S}$  increase with the increment of  $\text{SiO}$  abundance in these sources. Shock chemistry might be needed for further modeling.

#### 3.4. Line profiles

In most cases, the lines are very well fitted with a single Gaussian (see Figure 1 and A.1). This is especially apparent in  $\text{H}_2^{34}\text{S}$ ,  $\text{H}_2\text{CS}$ ,  $\text{HCS}^+$  and  $\text{HC}_3\text{N}$ , except for  $\text{H}_2\text{S}$  and  $\text{SiO}$ . The values of full width at half maxima (FWHM) are similar to each other for  $\text{H}_2^{34}\text{S}$ ,  $\text{H}_2\text{CS}$ ,  $\text{HCS}^+$  and  $\text{HC}_3\text{N}$  lines in each source, which are between  $1 \text{ km s}^{-1}$  and  $10 \text{ km s}^{-1}$  in all sources (see Table C.1), except for G000.67-00.03 (Sgr B2) and G043.16+000.01 (W49N). Figure 5 shows comparison among the FWHMs of the observed lines, for which the correlation is perfect between  $\text{HCS}^+$  and  $\text{H}_2\text{CS}$  with Pearson correlation coefficient of 0.98, good between  $\text{H}_2\text{CS}$  and  $\text{H}_2^{34}\text{S}$  (0.94),  $\text{HCS}^+$  and  $\text{H}_2^{34}\text{S}$  (0.95),  $\text{HCS}^+$  and  $\text{HC}_3\text{N}$  (0.92). Such results indicate that these observed  $\text{H}_2^{34}\text{S}$ ,  $\text{H}_2\text{CS}$ ,  $\text{HCS}^+$  and  $\text{HC}_3\text{N}$  transitions trace the same gas.

<sup>3</sup> The Pearson correlation coefficient is a measure of the linear relationship between two variables. The closer  $|r|$  is to 1, the stronger the linear relationship.

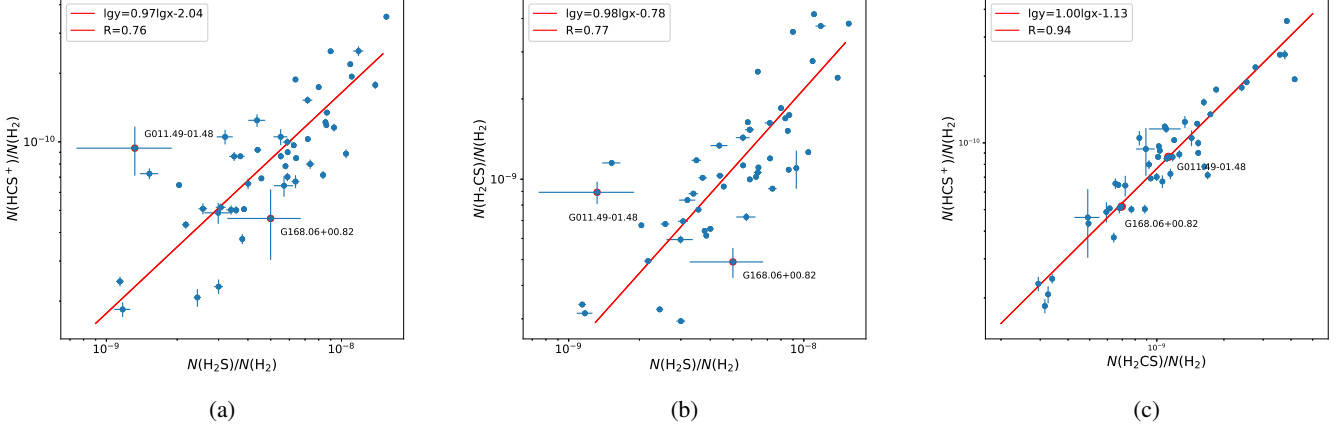


Fig. 2: The relationship among  $\text{H}_2\text{S}$ ,  $\text{H}_2\text{CS}$  and  $\text{HCS}^+$  molecules normalized by  $\text{H}_2$ . (a) shows the relationship between  $\text{HCS}^+$  and  $\text{H}_2\text{S}$  abundances. And (b) shows relationship between the  $\text{HCS}^+$  and  $\text{H}_2\text{S}$  abundances, while (c) prints the relationship between  $\text{HCS}^+$  and  $\text{H}_2\text{CS}$  abundances. The fitting lines are marked in red, using the least square method. G011.49-01.48 and G0168.06+00.82, which have large errors, are also marked, where  $\text{H}_2^{34}\text{S}$  lines showed weak emission.

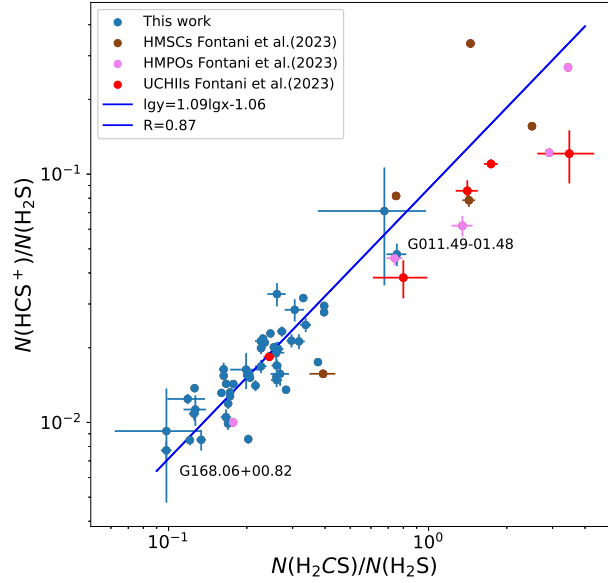


Fig. 3: The distribution of  $\text{H}_2\text{CS}$  and  $\text{HCS}^+$  molecular abundances in each source. Two sources (G011.49-01.48 and G0168.06+00.82) with large errors due to weak emission of  $\text{H}_2^{34}\text{S}$  lines. The molecular abundance ratios from Fontani et al. (2023) are also presented.

## 4. Discussion

### 4.1. Possible chemical connections between $\text{H}_2\text{S}$ , $\text{H}_2\text{CS}$ , and $\text{HCS}^+$ in hot cores?

S-bearing species are good tracers of hot cores because they are particularly sensitive to physical and chemical changes in dense and hot regions (Hatchell et al. 1998).  $\text{H}_2\text{S}$  is the main molecular form of S-bearing molecules in molecular clouds, which may be produced on the surface of grains, and the rapid reactions of  $\text{H}_2\text{S}$  molecules can drive the production of other S-bearing molecules (Druard & Wakelam 2012). The measured abundances of  $\text{H}_2\text{S}:\text{H}_2\text{CS}:\text{HCS}^+$  in these 50 sources showed that

$\text{H}_2\text{S}$  is the most abundant molecule with respect to  $\text{H}_2\text{S}$ ,  $\text{H}_2\text{CS}$  and  $\text{HCS}^+$ , what is found for  $\text{H}_2\text{O}$ , more abundant than  $\text{H}_2\text{CO}$ , and  $\text{HCO}^+$  (Herbst & Klemperer 1973).

The abundances of  $\text{HCS}^+$  and  $\text{H}_2\text{CS}$  presented even tighter correlation than that of these two molecules and  $\text{H}_2\text{S}$  with correlation coefficient of 0.94 (see Figure 2c). This is likely due to different chemical formation processes of  $\text{H}_2\text{S}$  compared to  $\text{HCS}^+$  and  $\text{H}_2\text{CS}$  in chemical models.  $\text{H}_2\text{S}$  is mainly formed on the grain surface (Druard & Wakelam 2012), while the other two molecules are primarily formed in the gas phase (Vidal & Wakelam 2018; Gronowski & Kołos 2014). Additionally, the elemental carbon also affects the formation of  $\text{H}_2\text{CS}$  and  $\text{HCS}^+$ , which

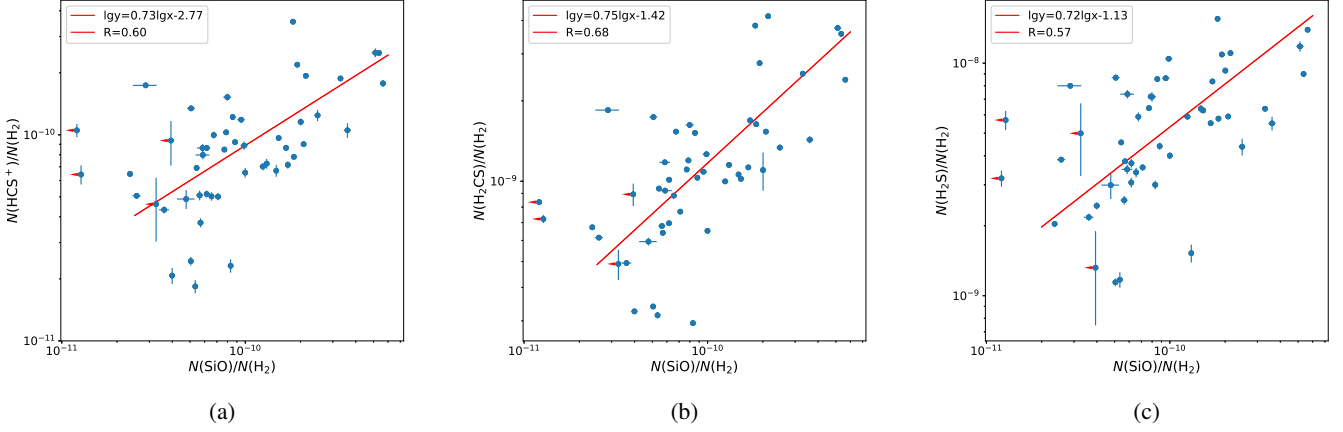


Fig. 4: The relationship between the three molecules and SiO, which use  $H_2$  to normalize. (a) shows the relationship between  $HCS^+$  and SiO abundances. And (b) shows relationship between the  $H_2CS$  and SiO abundances, while (c) shows the relationship between  $H_2S$  and SiO abundances. The fitting lines are marked in red, using the least square method. The four points marked with red arrows are realistic upper limits of SiO, which are no involvement in fitting.

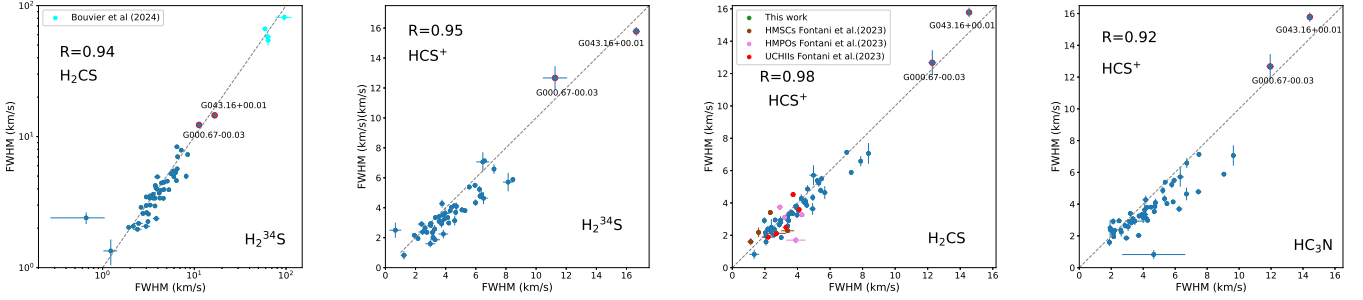


Fig. 5: Comparison among the lines FWHMs of the observed species. In all plots, the two blue points with red circles that are far away are G000.67-00.03 (Srg B2) and G043.16+000.01 (W49N). The number in the upper left corner of each panel is the Pearson  $\rho$  correlation coefficient. The gray line is  $y=x$ . The ratios from Bouvier et al. (2024) and Fontani et al. (2023) are also presented.

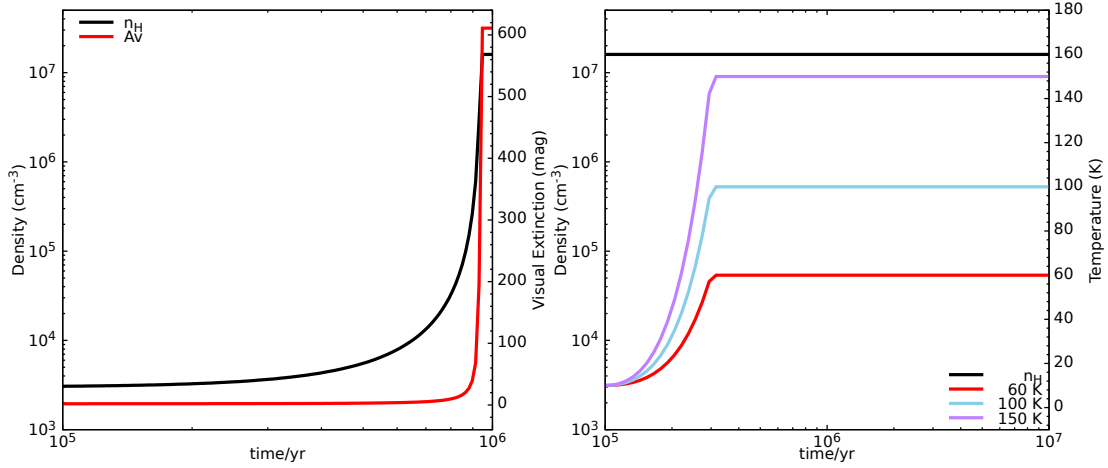


Fig. 6: The density, temperature, and  $A_V$  profiles as functions of time for collapse and warm-up stages in hot core models. The left panel represents the collapse stage, during the stage, the gas density gradually increases from  $3 \times 10^3 \text{ cm}^{-3}$  to  $1.6 \times 10^7 \text{ cm}^{-3}$  over a period of  $1 \times 10^6$  years, and the temperature remains at a constant value of 10 K. An increase in gas density leads to an increase in visual extinction. The right panel represents the warm-up stage, during the stage, the gas density and visual extinction are  $1.6 \times 10^7 \text{ cm}^{-3}$  and  $6.109 \times 10^2 \text{ mag}$ , respectively,  $T_{max}$  adopt three values, 60, 100 and 150K.

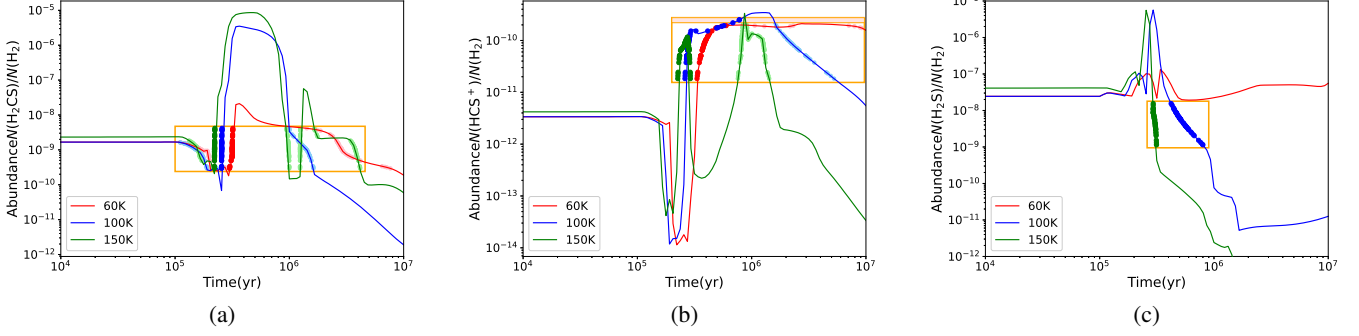


Fig. 7: Chemical model including includes the gas, the dust grain surface and the icy mantle. The solid lines correspond to the gas phase abundances versus time during warm-up stages in chemical models with gas maximum temperatures at 60, 100, and 150K, and the points are the observed datas. The abundances of  $\text{H}_2\text{CS}$ ,  $\text{HCS}^+$  and  $\text{H}_2\text{S}$ , relative to  $\text{H}_2$ , are presented in (a), (b) and (c), respectively. Since the samples are in the same evolutionary stage, two possible time are marked with filled and transparent circles from model. Note that there are no intersections for  $\text{H}_2\text{S}$  at 60K in model.

can reflect to the better correlation of  $\text{HCS}^+$  v.s.  $\text{H}_2\text{CS}$  than that of  $\text{HCS}^+$  v.s.  $\text{H}_2\text{S}$  and  $\text{H}_2\text{CS}$  v.s.  $\text{H}_2\text{S}$  in observation. Not only the correlation coefficients, but also the slopes of fitting results can be used to justify the relation between the abundances two molecules. We find a tight linear relationship between  $\text{HCS}^+$  and  $\text{H}_2\text{CS}$  with slope of 1.00, while that of the other two are 0.98 for  $\text{H}_2\text{CS}$  v.s.  $\text{H}_2\text{S}$  and 0.97 for  $\text{HCS}^+$  v.s.  $\text{H}_2\text{S}$ .

Our sample included 51 massive star forming regions at late stage, while the sample in Fontani et al. (2023) (see Figure 3) included 15 sources at different stages. The  $\text{HCS}^+/\text{H}_2\text{S}$  v.s.  $\text{H}_2\text{CS}/\text{H}_2\text{S}$  trend found in this work is also followed by the sources observed in Fontani et al. (2023). The line widths and excitation temperatures were obtained to explain that  $\text{HCS}^+$  trace preferentially quiescent and likely extended material. Our results showed that line widths of  $\text{H}_2^{34}\text{S}$ ,  $\text{H}_2\text{CS}$ ,  $\text{HCS}^+$  and  $\text{HC}_3\text{N}$  lines in each source were almost the same (see Figure 5), which indicate that they may be from the same gas.

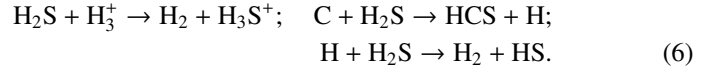
#### 4.2. Chemical model including gas, dust grain surface and icy mantle phases, for $\text{H}_2\text{S}$ , $\text{H}_2\text{CS}$ , and $\text{HCS}^+$ molecules

In order to understand the observed abundances of  $\text{H}_2\text{S}$ ,  $\text{H}_2\text{CS}$  and  $\text{HCS}^+$  in hot cores, we utilize the three-phase NAUTILUS chemical code (Ruaud et al. 2016), including gas, dust grain surface and icy mantle. This is combined with a similar physical model in Zhang et al. (2023), where a collapse stage is followed by a warm-up stage. During the collapse stage, the gas density is initially set at  $3 \times 10^3 \text{ cm}^{-3}$  and gradually increases to the final density  $1.6 \times 10^7 \text{ cm}^{-3}$  over a period of  $1 \times 10^6$  years. The gas temperatures are fixed at 10 K during this stage. The density gradually increases over time, resulting in an increase in extinction, as shown in the left panel of Fig 6. Once the peak density is achieved, the density is fixed and the gas and dust temperatures are raised from  $\sim 10$  K to their peak temperatures in  $2 \times 10^5$  years during the warm-up stages, as shown in the right panel of Fig 6. The main physical parameters of hot core models are summarized in Table 3. For our simulations, the initial abundances are those of Table 1 of Vidal & Wakelam (2018). The chemical network is based on the research work of Vidal et al. (2017).

In warm-up stage,  $\text{H}_2\text{S}$  is mainly formed through the following hydrogenation reactions on grain surfaces:



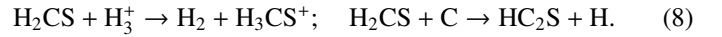
Some  $\text{H}_2\text{S}$  is already released back into the gas phase through reactive desorption before temperature rising. When the temperature reaches high values after  $2 \times 10^5$  yr, it can return to the gas phase through thermal process, which plays a dominant role in the production of gaseous  $\text{H}_2\text{S}$ . Initially,  $\text{H}_2\text{S}$  is mainly destroyed by  $\text{H}_3^+$  via ion-neutral reactions in all cases. However, after  $2 \times 10^5$  yr,  $7 \times 10^5$  yr, and  $3 \times 10^5$  yr, it is mainly destroyed by atomic carbon for a  $T_{\text{max}}$  of 60 and 100 K, and by atomic hydrogen for  $T_{\text{max}}$  of 150 K in the gas phase, respectively. The related reactions are as follows:



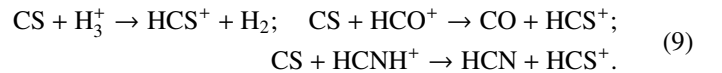
$\text{H}_2\text{CS}$  is primarily formed in gas phase through the following neutral-neutral reaction:



and it follows a similar destruction pathway to  $\text{H}_2\text{S}$ , as both are initially broken down through the ion  $\text{H}_3^+$ . After  $5 \times 10^5$  yr,  $7 \times 10^5$  yr and  $9 \times 10^5$  yr, respectively, in the gas phase, it is mainly destroyed by atomic carbon for  $T_{\text{max}}$  of 60, 100, and 150 K, respectively. The reactions proceed as follows:



Initially,  $\text{HCS}^+$  is mainly formed through the reaction of  $\text{CS}$  with the  $\text{H}_3^+$  ion in all cases. However, after  $3 \times 10^5$  yr and  $7 \times 10^5$  yr, it is primarily produced via the reactions  $\text{CS} + \text{HCO}^+$  and  $\text{CS} + \text{HCNH}^+$  for  $T_{\text{max}}$  of 60 and 150 K, respectively. The related reactions are as follows:



It is mainly destroyed in gas phase by the following electron recombination:



Both  $\text{H}_2\text{S}$  and  $\text{H}_2\text{CS}$  can be destroyed by the reactions with  $\text{H}_3^+$  (see Eq. (6) and (8)), while it is the main formation path of  $\text{HCS}^+$  by reaction with  $\text{H}_3^+$  (see Eq. (9)). The relation of  $\text{H}_2\text{S}$ ,  $\text{H}_2\text{CS}$  and  $\text{HCS}^+$  with  $\text{H}_3^+$  can cause close connection among them.

If we compare with the similar O-bearing species,  $\text{H}_2\text{CO}$  could be produced from  $\text{H}_2\text{O}+\text{CO}$ , and is the second most abundant product after  $\text{CO}_2$ , at different concentrations of  $\text{H}_2\text{O}:\text{CO}$  mixtures (de Barros et al. 2022). There are other processes to form  $\text{H}_2\text{CO}$  from  $\text{H}_2\text{O}$ , such as  $\text{H}_2\text{O}+\text{C} \rightarrow \text{H}_2\text{CO}$  at temperatures associated with ISM and the cooler regions of the environment around young stars (Potapov et al. 2021). It shows that  $\text{H}_2\text{CO}$  is formed in a different way with  $\text{H}_2\text{CS}$ . The formation of  $\text{HCO}^+$  under different  $A_v$  is different. From  $A_v \sim 0.4$  to 3, the dominant reaction is  $\text{CO}^+ + \text{H}_2$ , while above 3, the dominant reaction is  $\text{H}_3^+ + \text{CO}$  in molecular clouds (Panessa et al. 2023).  $\text{HCO}^+$  can be destroyed by  $\text{C}_3\text{H}_2$  (Narita et al. 2024). The formation paths of  $\text{HCO}^+$  and  $\text{HCS}^+$  seem to be the same in particular cases.

Considering processes including what have been described before, the results of relative abundances of  $\text{H}_2\text{S}$ ,  $\text{H}_2\text{CS}$  and  $\text{HCS}^+$  species in gas phase varying with the time for warm-up stages from the model are presented in Figure 7, with three different maximum temperatures ( $T_{max}$ ) as 60K, 100 K and 150K. The measured abundances are compared with the abundances from the model, which can have same value at different time (see Figure 7). Since the samples are in the same evolutionary stage, the more reasonable intersections are marked with filled circles. Transparent circles show another possible time. We considered the calculated abundance consistent with the observed value if the calculated abundance differs from the observed value within one order of magnitude value.

For  $T_{max}=60\text{K}$  (see Figure 7, red lines), the abundance of  $\text{H}_2\text{S}$  and  $\text{H}_2\text{CS}$  varies much less than that of  $\text{HCS}^+$ . Besides, there is one possible time ( $3 \times 10^5$  yr) for each source that match the measured  $[\text{H}_2\text{CS}/\text{H}_2]$  and  $[\text{HCS}^+/\text{H}_2]$  (red line and filled circles) abundances (see Figure 7a, 7b), while no intersection for  $[\text{H}_2\text{S}/\text{H}_2]$  (see Figure 7c). However, the discrepancy is less one order of magnitude. Comparing to the observational results, the over prediction of  $\text{H}_2\text{S}$  that we find could be a result of the absence of effective gas-phase destruction reactions in the  $\text{H}_2\text{S}$  chemistry within our model.  $[\text{HCS}^+/\text{H}_2]$  abundances in all sources range from  $1.84 \times 10^{-11}$  to  $3.54 \times 10^{-10}$ , and four of them are above the model results from  $2.19 \times 10^{-10}$  to  $3.54 \times 10^{-10}$  (see Figure 7b, orange rectangle box with fill), while all sources with measured  $[\text{H}_2\text{CS}/\text{H}_2]$  abundances, from  $2.94 \times 10^{-10}$  to  $4.15 \times 10^{-9}$ , are matched the model results.

The abundances of  $\text{H}_2\text{CS}$  and  $\text{HCS}^+$  changes quickly than  $\text{H}_2\text{S}$  in  $1 \times 10^5$  to  $1 \times 10^7$  yr, with  $T_{max}=100\text{K}$  (see Figure 7, blue lines). There is not a single time for comparisons between the observed value and the model. The solutions are totally different for different molecules (see Figure 7), with about  $2 \times 10^5$  yr for  $[\text{H}_2\text{CS}/\text{H}_2]$ ,  $3 \times 10^5$  yr for  $[\text{HCS}^+/\text{H}_2]$  and  $5 \times 10^5$  yr for  $[\text{H}_2\text{S}/\text{H}_2]$ .

The possible time with  $T_{max}=150\text{K}$  for each source to match the measured abundances of  $[\text{H}_2\text{S}/\text{H}_2]$  is concentrated around  $3 \times 10^5$  yr (see Figure 7c, green lines). For the two to four possible solutions of time in each source for  $[\text{H}_2\text{CS}/\text{H}_2]$  and  $[\text{HCS}^+/\text{H}_2]$ , it is more likely to be the younger one for most of the sources, with one time for each to explain the three different abundances in each source, around  $3 \times 10^5$  yr.

In general, the models can reproduce the observed abundances at around  $2-3 \times 10^5$  yr for almost all of the sources. However, there are small discrepancy at lower  $T_{max}$  (60K) models for  $\text{H}_2\text{S}$ .  $\text{H}_2\text{CS}$  and  $\text{HCS}^+$  can be efficiently formed in gas-phase, while  $\text{H}_2\text{S}$  already chemically desorbs during its formation on

the grains before being thermally desorbed. The abundance of  $\text{H}_2\text{S}$  cannot sharply increase like at  $T_{max}$  of 100K and 150K after the temperature reaches  $T_{max}$  of 60K because it does not reach the desorption temperature of  $\text{H}_2\text{S}$  (around 70K). In this condition, the chemical desorption is primary origin for gaseous  $\text{H}_2\text{S}$ . Since gas-phase destruction reactions for  $\text{H}_2\text{S}$  are not as effective at relatively low temperature of 60K compared to  $T_{max}$  of 100K and 150K, the abundance of  $\text{H}_2\text{S}$  is over predicted in our model.

### 4.3. Shock activities

$\text{SiO}$  was considered to be an excellent tracer of shock activities in star formation regions, because  $\text{SiO}$  abundance in molecular outflows was increased by at least three orders of magnitude compared to those in quiescent gas (Schilke et al. 1997). Lots of elemental Si were probably to be found in the form of stable materials in dust, like silicates, which were difficult to release Si atoms. Shock activities were needed to destroy silicates to release Si atoms from the grains into gas phase (Martin-Pintado et al. 1992), while S-bearing molecules can be enhanced with moderate shocks (Wakelam et al. 2004).

$\text{SiO}$  4-3 was detected in 46 of 51 sources in our sample (see green lines in Figure 1 (d), (e) and (f)), indicating shock activities there. The abundances of  $\text{HCS}^+$ ,  $\text{H}_2\text{CS}$ , and  $\text{H}_2\text{S}$  increase with the increment of  $\text{SiO}$  abundance in these sources (see Figure 4), which implies that shock chemistry may be important for  $\text{HCS}^+$ ,  $\text{H}_2\text{CS}$ , and  $\text{H}_2\text{S}$ . In addition, the line width of  $\text{SiO}$  is larger than those of the S-bearing species. This may indicate that the  $\text{SiO}$  is actually tracing a different physical component with a different velocity broadening. Indeed,  $\text{SiO}$  likely traces shocked regions, which implies that the S-bearing species are either tracing weaker shocks not traced by  $\text{SiO}$  or are actually tracing the hot core regions.

## 5. Summary and conclusions

We have observed  $\text{H}_2\text{S}$   $1_{10-1_{01}}$ ,  $\text{H}_2^{34}\text{S}$   $1_{10-1_{01}}$ ,  $\text{H}_2\text{CS}$   $5_{14-4_{14}}$ ,  $\text{HCS}^+$  4-3,  $\text{HC}_3\text{N}$  19-18,  $\text{SiO}$  4-3 and  $\text{C}^{18}\text{O}$  1-0 towards a sample of 51 massive star forming regions with the IRAM 30-m millimeter telescope. We have obtained beam average column densities, as well as their abundances with respect to  $\text{H}_2$ , derived from  $\text{C}^{18}\text{O}$ .

All lines can be well fitted with a single Gaussian, except for  $\text{H}_2\text{S}$  and  $\text{SiO}$ . The values of FWHMs are between  $1 \text{ km s}^{-1}$  and  $10 \text{ km s}^{-1}$  in all sources, except for G000.67-00.03 (Srg B2) and G043.16+000.01 (W49N). Comparing among the lines FWHMs of the observed species, we find that they are positively correlated with each other, as well as they have similar FWHM ranges, which indicate that they may trace similar regions.

The abundance ratios of  $[\text{H}_2\text{S}/\text{H}_2]$ ,  $[\text{H}_2\text{CS}/\text{H}_2]$  and  $[\text{HCS}^+/\text{H}_2]$  range by more than one magnitude with high correlation coefficients and positive slopes between them, with correlation coefficient of 0.94, slope of 1.00 for  $[\text{H}_2\text{CS}/\text{H}_2]$  and  $[\text{HCS}^+/\text{H}_2]$ , while the correlation coefficient and slope between  $[\text{H}_2\text{S}/\text{H}_2]$  and  $[\text{HCS}^+/\text{H}_2]$  are 0.76 and 0.97, respectively. For  $[\text{H}_2\text{CS}/\text{H}_2]$  and  $[\text{H}_2\text{S}/\text{H}_2]$ , the correlation coefficients and slope are 0.77 and 0.98. The close relations indicate that these S-bearing molecules may have chemical connections with each others, with  $\text{HCS}^+$  and  $\text{H}_2\text{CS}$  the most correlated ones, based on the relations between the relative abundances of these molecules in the 50 sources.

The three-phase NAUTILUS chemical code was utilized to simulate the relationship of three S-bearing molecules. Comparing the observed abundance with model results, there are one

possible time ( $2\text{--}3\times 10^5$  yr) for each source in the model to match the measured abundances of  $\text{H}_2\text{S}$ ,  $\text{H}_2\text{CS}$  and  $\text{HCS}^+$ . The abundances of  $\text{HCS}^+$ ,  $\text{H}_2\text{CS}$ , and  $\text{H}_2\text{S}$  increase with the increment of SiO abundance in these sources, which implies that shock chemistry may be important for them. Shock activity need to be considered in further modeling  $\text{H}_2\text{S}$ ,  $\text{H}_2\text{CS}$  and  $\text{HCS}^+$  in hot cores.

*Acknowledgements.* This work is supported by National Key R&D Program of China (2023YFA1608204) and the National Natural Science Foundation of China grant 12173067. This study is based on observations carried out under project number 012-16, 023-17 and 005-20 with the IRAM 30m telescope. IRAM is supported by INSU/CNRS (France), MPG (Germany) and IGN (Spain).

## References

- Adande, G. R., Halfen, D. T., Ziurys, L. M., et al. 2010, *ApJ*, 725, 561  
 Asplund, M., Grevesse, N., & Sauval, A. J. 2005, *Cosmic Abundances as Records of Stellar Evolution and Nucleosynthesis*, 336, 25  
 Blake, G. A., Sutton, E. C., Masson, C. R., et al. 1987, *ApJ*, 315, 621  
 Bonfand, M., Belloche, A., Garrod, R. T., et al. 2019, *A&A*, 628, A27  
 Bouscasse, L., Csengeri, T., Belloche, A., et al. 2022, *A&A*, 662, A32  
 Bouvier, M., Viti, S., Behrens, E., et al. 2024, *A&A*, 689, A64  
 Brown, R. D., Godfrey, P. D., & Winkler, D. A. 1980, *MNRAS*, 190, 1  
 Cernicharo, J., Guélin, M., & Kahane, C. 2000, *A&AS*, 142, 181  
 Charnley, S. B. 1997, *ApJ*, 481, 396  
 Chin, Y.-N., Henkel, C., Whiteoak, J. B., et al. 1996, *A&A*, 305, 960  
 Coutens, A., Willis, E. R., Garrod, R. T., et al. 2018, *A&A*, 612, A107  
 Drdla, K., Knapp, G. R., & van Dishoeck, E. F. 1989, *ApJ*, 345, 815  
 Druard, C. & Wakelam, V. 2012, *MNRAS*, 426, 354  
 de Barros, A. L. F., Mejía, C., Seperuelo Duarte, E., et al. 2022, *MNRAS*, 511, 2491  
 Esplugues, G. B., Tercero, B., Cernicharo, J., et al. 2013, *A&A*, 556, A143  
 Esplugues, G. B., Viti, S., Goicoechea, J. R., et al. 2014, *A&A*, 567, A95  
 Esplugues, G., Fuente, A., Navarro-Almáida, D., et al. 2022, *A&A*, 662, A52  
 Esplugues, G., Rodríguez-Baras, M., San Andrés, D., et al. 2023, *A&A*, 678, A199  
 Frerking, M. A., Linke, R. A., & Thaddeus, P. 1979, *ApJ*, 234, L143  
 Frerking, M. A., Langer, W. D., & Wilson, R. W. 1982, *ApJ*, 262, 590  
 Fontani, F., Roueff, E., Colzi, L., et al. 2023, *A&A*, 680, A58  
 el Akel, M., Kristensen, L. E., Le Gal, R., et al. 2022, *A&A*, 659, A100  
 Garozzo, M., Fulvio, D., Kanuchova, Z., et al. 2010, *A&A*, 509, A67  
 Garrod, R. T. & Herbst, E. 2006, *A&A*, 457, 927  
 Goldsmith, P. F. & Linke, R. A. 1980, , 81  
 Goldsmith, P. F. & Langer, W. D. 1999, *ApJ*, 517, 209  
 Gronowski, M. & Kotos, R. 2014, *ApJ*, 792, 89  
 Gottlieb, C. A., Gottlieb, E. W., Litvak, M. M., et al. 1978, *ApJ*, 219, 77  
 Gudeman, C. S., Haese, N. N., Piltch, N. D., et al. 1981, *ApJ*, 246, L47  
 Hatchell, J., Thompson, M. A., Millar, T. J., et al. 1998, *A&A*, 338, 713  
 Herbst, E. & Klemperer, W. 1973, *ApJ*, 185, 505  
 Inostroza-Pino, N., Palmer, C. Z., Lee, T. J., et al. 2020, *Journal of Molecular Spectroscopy*, 369, 111273  
 Jenkins, E. B. 2009, *ApJ*, 700, 1299  
 Jiménez-Escobar, A. & Muñoz Caro, G. M. 2011, *A&A*, 536, A91  
 Kalenskii, S. V., Slysh, V. I., & Val'ts, I. E. 2002, *Astronomy Reports*, 46, 96  
 Kalenskii, S. V., Kaiser, R. I., Bergman, P., et al. 2022, *ApJ*, 932, 5  
 Li, J., Wang, J., Zhu, Q., et al. 2015, *ApJ*, 802, 40  
 Li, Y., Wang, J., Li, J., et al. 2022, *MNRAS*, 512, 4934  
 Lis, D. C., Goldsmith, P. F., Güsten, R., et al. 2023, *A&A*, 669, L15  
 Luo, G., Feng, S., Li, D., et al. 2019, *ApJ*, 885, 82  
 Martín-Pintado, J., Bachiller, R., & Fuente, A. 1992, *A&A*, 254, 315  
 McClure, M. K., Rocha, W. R. M., Pontoppidan, K. M., et al. 2023, *Nature Astronomy*, 7, 431  
 Miessler, G. L., Fischer, P. J., Tarr, D. A. 2013, *Inorganic Chemistry (Fifth Edition)*, ISBN: 0-321-81105-4  
 Minh, Y. C., Ziurys, L. M., Irvine, W. M., et al. 1991, *ApJ*, 366, 192  
 Montaigne, H., Geppert, W. D., Semaniak, J., et al. 2005, *ApJ*, 631, 653  
 Müller, H. S. P., Thorwirth, S., Roth, D. A., et al. 2001, *A&A*, 370, L49  
 Müller, H. S. P., Schlöder, F., Stutzki, J., et al. 2005, *Journal of Molecular Structure*, 742, 215  
 Navarro-Almáida, D., Le Gal, R., Fuente, A., et al. 2020, *A&A*, 637, A39  
 Narita, K., Sakamoto, S., Koda, J., et al. 2024, *ApJ*, 969, 102  
 Neufeld, D. A., Godard, B., Gerin, M., et al. 2015, *A&A*, 577, A49  
 Panessa, M., Seifried, D., Walch, S., et al. 2023, *MNRAS*, 523, 6138  
 Potapov, A., Krasnokutski, S. A., Jäger, C., et al. 2021, *ApJ*, 920, 111  
 Reid, M. J., Menten, K. M., Brunthaler, A., et al. 2014, *ApJ*, 783, 130  
 Reid, M. J., Pesce, D. W., & Riess, A. G. 2019, *ApJ*, 886, L27  
 Ruaud, M., Wakelam, V., & Hersant, F. 2016, *MNRAS*, 459, 3756  
 Santos, J. C., Linnartz, H., & Chuang, K.-J. 2023, *A&A*, 678, A112  
 Schilke, P., Walmsley, C. M., Pineau des Forets, G., et al. 1997, *A&A*, 321, 293  
 Schwartz, P. R., Zuckerman, B., & Bologna, J. M. 1982, *ApJ*, 256, L55  
 Shingledecker, C. N., Lamberts, T., Laas, J. C., et al. 2020, *ApJ*, 888, 52  
 Thaddeus, P., Kutner, M. L., Penzias, A. A., et al. 1972, *ApJ*, 176, L73  
 Turner, B. E. 1989, *ApJS*, 70, 539  
 Tychoniec, Ł., van Dishoeck, E. F., van't Hoff, M. L. R., et al. 2021, *A&A*, 655, A65  
 Ulich, B. L. & Haas, R. W. 1976, *ApJS*, 30, 247  
 van der Tak, F. F. S., Black, J. H., Schöier, F. L., et al. 2007, *A&A*, 468, 627  
 van Dishoeck, E. F., Kristensen, L. E., Mottram, J. C., et al. 2021, *A&A*, 648, A24  
 Vidal, T. H. G., Loison, J.-C., Jaziri, A. Y., et al. 2017, *MNRAS*, 469, 435  
 Vidal, T. H. G. & Wakelam, V. 2018, *MNRAS*, 474, 5575  
 Wakelam, V., Castets, A., Ceccarelli, C., et al. 2004, *A&A*, 413, 609  
 Yan, Y. T., Henkel, C., Kobayashi, C., et al. 2023, *A&A*, 670, A98  
 Zhang, X., Quan, D., Li, R., et al. 2023, *MNRAS*, 521, 1578

Table 1: Information of the sources and detected lines.

Source name Alias	RA(J2000) (hh : mm : ss)	DEC(J2000) (dd : mm : ss)	$D_{GC}$ (kpc)	Line	$\int T_{mb} dv$ (K km s <sup>-1</sup> )	$v_{LSR}$ (km s <sup>-1</sup> )	$T_{peak}$ (K)
G121.29+00.65 L1287	00:36:47.35	63:29:02.2	8.8	HC <sub>3</sub> N (19-18)	1.92±0.03	-17.4±0.1	0.69
				<sup>a</sup> H <sub>2</sub> S (1 <sub>10</sub> -1 <sub>01</sub> )	9.08±0.04	-17.7±0.1	2.03
				H <sub>2</sub> <sup>34</sup> S (1 <sub>10</sub> -1 <sub>01</sub> )	0.69±0.03	-17.5±0.1	0.24
				<sup>a</sup> H <sub>2</sub> CS (5 <sub>14</sub> -4 <sub>14</sub> )	2.27±0.02	-17.4±0.1	0.81
				HCS <sup>+</sup> (4-3)	0.93±0.02	-17.5±0.1	0.37
				<sup>a</sup> C <sup>18</sup> O (1-0)	7.06±0.02	-17.6±0.1	2.51
				SiO (4-3)	1.68±0.06	-17.1±0.1	0.42
G123.06-06.30 NGC281	00:52:24.70	56:33:50.5	10.1	HC <sub>3</sub> N (19-18)	2.77±0.03	-30.8±0.1	0.81
				H <sub>2</sub> S (1 <sub>10</sub> -1 <sub>01</sub> )	10.40±0.03	-31.0±0.1	2.07
				H <sub>2</sub> <sup>34</sup> S (1 <sub>10</sub> -1 <sub>01</sub> )	0.95±0.02	-30.5±0.1	0.26
				H <sub>2</sub> CS (5 <sub>14</sub> -4 <sub>14</sub> )	4.70±0.02	-30.4±0.1	1.24
				HCS <sup>+</sup> (4-3)	1.68±0.03	-30.6±0.1	0.46
				<sup>a</sup> C <sup>18</sup> O (1-0)	5.87±0.03	-30.0±0.1	1.62
				SiO (4-3)	7.50±0.08	-31.0±0.1	0.42

Notes. More information is presented in Zenodo. <https://doi.org/10.5281/zenodo.13937627>

Table 2: Spectroscopic information from CDMS.

Line <sup>(a)</sup>	Frequency(MHz)	$A_{ul}(s^{-1})$	Q( $T_{ex}=18.75K$ )	$g_u$	$E_u(cm^{-1})$	Ref. <sup>(b)</sup>
HC <sub>3</sub> N 19-18	172849.300	$4.08 \times 10^{-4}$	86.2	39	27.88	(Kalenskii et al. 2002)
H <sub>2</sub> <sup>34</sup> S 1 <sub>10</sub> -1 <sub>01</sub>	167910.516	$2.64 \times 10^{-5}$	8.72	9	27.83	(Minh et al. 1991)
H <sub>2</sub> CS 5 <sub>14</sub> -4 <sub>14</sub>	169114.160	$6.68 \times 10^{-5}$	91.2	33	37.54	(Thaddeus et al. 1972)
HCS <sup>+</sup> 4-3	170691.603	$9.86 \times 10^{-5}$	18.7	9	20.48	(Gudeman et al. 1981)
SiO 4-3	173688.274	$2.61 \times 10^{-4}$	18.3	9	20.84	(Schwartz et al. 1982)
C <sup>18</sup> O 1-0	109782.173	$6.27 \times 10^{-8}$	7.46	3	5.27	(Ulich & Haas 1976)

Notes. <sup>a</sup> All parameters are taken from the CDMS catalogue, <sup>b</sup> Reference paper where the observations are presented.

Table 3: Physical parameters of hot core models.

Source(Stage)	$n_H(cm^{-3})$	T(K)	$A_V(mag)$	$\zeta(s^{-1})$	UV factor(Habing)
The free fall collapse <sup>a,b</sup>	$3 \times 10^3 \rightarrow 1.6 \times 10^7$	10	$2 \rightarrow 6.109 \times 10^2$	$1.3 \times 10^{-17}$	1
The warm-up <sup>b,c</sup>	$1.6 \times 10^7$	10 → 60, 100, 150	$6.109 \times 10^2$	$1.3 \times 10^{-17}$	1

Notes. <sup>a</sup> Garrod & Herbst (2006), <sup>b</sup> Bonfand et al. (2019), <sup>c</sup> Coutens et al. (2018)

Appendix A: Spectra for individual sources

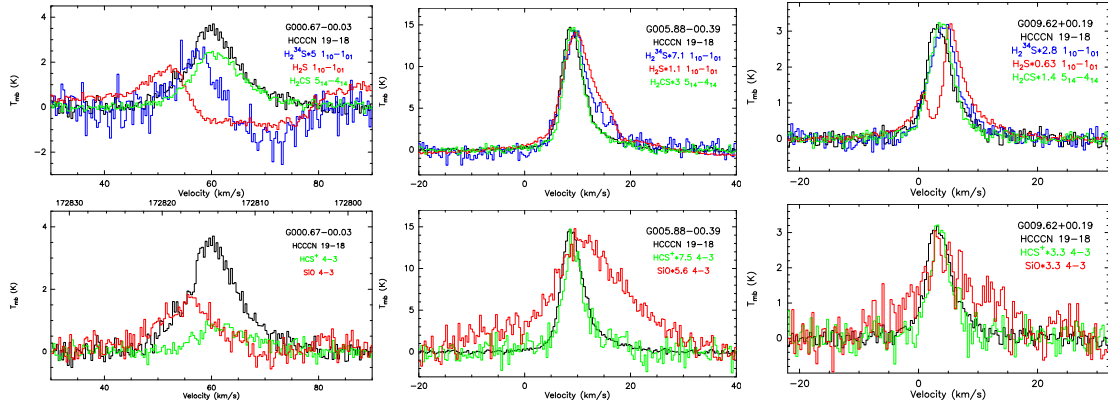


Fig. A.1: The same as Figure 1 for more sources. More figures are presented in Zenodo.  
<https://doi.org/10.5281/zenodo.13937627>

## Appendix B: Beam averaged column densities.

Table B.1: Beam averaged column densities.

Source	<sup>b</sup> N(H <sub>2</sub> S) 10 <sup>14</sup> cm <sup>-2</sup>	<sup>c</sup> N(H <sub>2</sub> S) 10 <sup>14</sup> cm <sup>-2</sup>	N(H <sub>2</sub> <sup>34</sup> S) 10 <sup>13</sup> cm <sup>-2</sup>	N(H <sub>2</sub> CS) 10 <sup>13</sup> cm <sup>-2</sup>	N(HCS <sup>+</sup> ) 10 <sup>12</sup> cm <sup>-2</sup>	N(HC <sub>3</sub> N) 10 <sup>14</sup> cm <sup>-2</sup>	N(SiO) 10 <sup>12</sup> cm <sup>-2</sup>	N(C <sup>18</sup> O) 10 <sup>16</sup> cm <sup>-2</sup>	N(H <sub>2</sub> ) 10 <sup>22</sup> cm <sup>-2</sup>
G000.67-00.03	<sup>a</sup> 39.7±0.9	7.31±0.65	4.39±0.39	55.3±0.20	34.8±1.9	10.7 ± 0.17	62.8±1.1	11.0±0.04	48.0±0.18
G005.88-00.39	29.1±0.2	22.9±0.41	11.2±0.20	39.5±0.61	29.2±1.1	20.4 ± 0.26	92.5±1.4	3.76±0.02	16.4±0.09
G009.62+00.19	<sup>a</sup> 17.7±0.1	12.3±0.31	6.49±0.16	20.8±0.27	14.6±0.6	4.47 ± 0.09	26.0±1.0	4.77±0.01	20.8±0.05
G010.47+00.02	<sup>a</sup> 45.4±0.3	26.5±0.42	15.0±0.24	65.3±0.28	60.4±1.8	11.8 ± 0.07	31.0±0.74	3.91±0.02	17.1±0.08
G010.62-00.38	<sup>a</sup> 49.6±0.2	35.0±0.31	18.3±0.16	62.1±0.14	49.9±0.7	10.0 ± 0.09	34.9±0.52	9.37±0.01	40.9±0.06
G011.49-01.48	1.11±0.02	0.36±0.16	0.17±0.07	2.43±0.23	2.55±0.62	0.87 ± 0.07	≤1.07	0.62±0.01	2.72±0.05
G011.91-00.61	<sup>a</sup> 4.72±0.20	3.54±0.14	1.75±0.07	5.88±0.14	3.72±0.24	1.40 ± 0.03	8.19±0.24	1.27±0.01	5.55±0.04
G012.80-00.20	<sup>a</sup> 8.44±0.03	6.50±0.12	3.17±0.06	21.4±0.13	20.6±0.2	4.77 ± 0.02	7.50±0.15	7.30±0.01	31.9±0.03
G012.88+00.48	<sup>a</sup> 10.1±0.08	7.05±0.10	3.39±0.05	14.5±0.11	10.7±0.2	1.85 ± 0.08	8.39±0.18	3.54±0.01	15.4±0.03
G012.90-00.26	<sup>a</sup> 8.34±0.07	6.38±0.15	3.07±0.07	10.8±0.15	6.31±0.32	2.40 ± 0.04	9.61±0.34	3.86±0.01	16.9±0.05
G014.33-00.64	<sup>a</sup> 8.29±0.13	6.80±0.33	3.12±0.15	21.6±0.37	14.4±0.7	3.00 ± 0.10	29.4±1.4	1.32±0.01	5.75±0.04
G015.03-00.67	<sup>a</sup> 2.54±0.02	2.15±0.20	1.01±0.09	2.72±0.09	2.42±0.26	2.05 ± 0.03	≤0.48	0.86±0.01	3.77±0.03
G016.58-00.05	<sup>a</sup> 5.58±0.05	4.15±0.13	2.06±0.06	8.96±0.11	5.84±0.23	1.25 ± 0.03	8.27±0.30	2.67±0.01	11.6±0.03
G023.00-00.41	<sup>a</sup> 4.94±0.06	3.61±0.13	1.83±0.06	4.82±0.11	3.08±0.27	1.32 ± 0.03	5.92±0.23	3.39±0.01	14.8±0.04
G023.44-00.18	2.98±0.05	2.15±0.08	1.12±0.04	6.39±0.12	4.59±0.22	0.74 ± 0.03	9.51±0.23	4.31±0.01	18.8±0.06
G027.36-00.16	8.09±0.06	5.86±0.11	3.03±0.05	16.6±0.15	7.94±0.25	2.35 ± 0.04	18.7±0.33	2.32±0.01	10.2±0.03
G028.86+00.06	6.44±0.05	4.60±0.09	2.37±0.05	7.34±0.09	6.05±0.16	1.08 ± 0.02	3.05±0.16	2.73±0.01	11.9±0.03
G029.95-00.01	21.8±0.1	16.0±0.25	8.07±0.12	19.4±0.24	13.6±0.6	3.85 ± 0.10	15.1±0.67	3.51±0.01	15.3±0.04
G031.28+00.06	<sup>a</sup> 5.67±0.12	4.04±0.19	1.00±0.09	13.6±0.17	9.98±0.44	1.40 ± 0.05	6.76±0.45	2.65±0.01	11.6±0.04
G031.58+00.07	<sup>a</sup> 4.72±0.05	3.50±0.16	1.74±0.08	9.12±0.15	5.19±0.24	0.97 ± 0.03	6.76±0.22	2.37±0.01	10.3±0.04
G032.04+00.05	<sup>a</sup> 7.16±0.05	5.33±0.12	2.66±0.06	10.9±0.11	8.35±0.29	1.67 ± 0.03	16.1±0.23	2.21±0.01	9.65±0.03
G034.39+00.22	0.98±0.01	0.83±0.06	0.38±0.03	2.23±0.06	1.30±0.10	0.27 ± 0.01	3.78±0.12	1.62±0.01	7.08±0.02
G035.02+00.34	<sup>a</sup> 6.27±0.03	5.01±0.10	2.36±0.05	8.33±0.08	7.16±0.17	1.76 ± 0.02	5.47±0.19	1.59±0.01	6.96±0.03
G035.19-00.74	<sup>a</sup> 6.17±0.04	5.06±0.22	2.37±0.10	13.2±0.13	8.57±0.32	2.73 ± 0.03	5.78±0.20	1.97±0.01	8.59±0.05
G035.20-01.73	4.24±0.02	3.37±0.14	1.62±0.07	4.22±0.09	3.65±0.17	0.35 ± 0.03	2.69±0.23	1.05±0.01	4.58±0.02
G037.43+01.51	1.89±0.01	1.62±0.07	0.75±0.03	4.27±0.09	3.19±0.17	0.62 ± 0.02	3.54±0.15	1.44±0.01	6.28±0.02
G043.16+00.01	<sup>a</sup> 18.3±0.09	15.5±0.22	7.04±0.10	25.3±0.17	23.9±0.5	7.10 ± 0.06	37.6±0.36	5.67±0.01	24.8±0.04
G043.79-00.12	<sup>a</sup> 5.42±0.03	4.28±0.15	2.07±0.07	10.0±0.11	8.99±0.25	1.14 ± 0.03	8.57±0.20	2.23±0.01	9.74±0.04
G049.48-00.36	16.3±0.09	13.3±0.19	6.28±0.09	26.9±0.06	11.4±0.5	8.16 ± 0.04	27.1±0.52	3.64±0.02	15.9±0.08
G049.48-00.38	<sup>a</sup> 43.2±0.1	33.2±0.25	15.8±0.12	125±0.16	58.2±1.0	15.3 ± 0.09	64.3±1.5	6.89±0.03	30.1±0.11
G059.78+00.06	3.09±0.02	2.60±0.07	1.18±0.03	6.00±0.07	5.65±0.17	0.63 ± 0.02	0.93±0.14	0.74±0.01	3.25±0.02
G069.54-00.97	<sup>a</sup> 2.79±0.02	2.40±0.12	1.08±0.05	5.45±0.08	4.04±0.15	1.45 ± 0.02	4.83±0.17	1.79±0.01	7.83±0.02
G075.76+00.33	<sup>a</sup> 3.84±0.01	3.44±0.11	1.53±0.05	6.91±0.05	5.34±0.14	1.04 ± 0.01	2.01±0.10	0.91±0.01	3.97±0.03
G078.12+03.63	1.67±0.01	1.51±0.10	0.67±0.05	3.92±0.12	2.89±0.23	1.66 ± 0.03	9.88±0.44	0.63±0.01	2.74±0.02
G081.75+00.59	1.85±0.03	1.63±0.06	0.72±0.03	3.70±0.05	3.24±0.13	0.78 ± 0.01	2.71±0.17	1.71±0.01	7.48±0.02
G081.87+00.78	7.59±0.04	6.72±0.12	2.99±0.05	17.5±0.12	10.3±0.3	4.19 ± 0.03	23.7±0.32	2.61±0.01	11.4±0.04
G092.67+03.07	2.93±0.02	2.60±0.07	1.15±0.03	10.3±0.07	7.22±0.13	1.43 ± 0.02	15.5±0.21	0.66±0.01	2.89±0.02
G109.87+02.11	<sup>a</sup> 3.39±0.01	3.09±0.13	1.36±0.06	3.03±0.06	2.38±0.18	2.34 ± 0.03	8.56±0.28	2.36±0.01	10.3±0.02
G111.54+00.77	<sup>a</sup> 4.42±0.03	4.13±0.06	1.76±0.02	7.13±0.05	5.47±0.10	0.81 ± 0.01	4.96±0.10	1.48±0.01	6.45±0.02
G121.29+00.65	<sup>a</sup> 1.54±0.01	1.41±0.06	0.62±0.03	3.85±0.03	3.28±0.07	0.50 ± 0.01	2.34±0.08	0.87±0.01	3.80±0.01
G123.06-06.30	2.13±0.01	2.01±0.04	0.84±0.02	7.98±0.04	5.93±0.09	0.73 ± 0.01	10.4±0.11	0.72±0.01	3.16±0.02
G133.94+01.06	<sup>a</sup> 9.99±0.04	8.85±0.15	3.74±0.06	22.5±0.12	17.8±0.2	2.66 ± 0.02	15.6±0.16	1.86±0.01	8.12±0.03
G168.06+00.82	<sup>a</sup> 0.64±0.03	0.72±0.25	0.26±0.08	0.71±0.09	0.67±0.22	0.17 ± 0.07	≤0.47	0.33±0.01	1.45±0.03
G176.51+00.20	<sup>a</sup> 0.78±0.01	0.73±0.09	0.31±0.04	1.45±0.05	1.19±0.12	0.20 ± 0.01	1.16±0.13	0.56±0.01	2.44±0.01
G183.72-03.66	0.52±0.01	0.50±0.04	0.21±0.02	1.52±0.04	1.41±0.09	0.21 ± 0.01	2.81±1.12	0.26±0.01	1.13±0.01
G188.94+00.88	1.87±0.01	1.82±0.09	0.75±0.04	4.11±0.07	3.86±0.15	0.26 ± 0.01	2.02±0.10	0.58±0.01	2.53±0.02
G192.60-00.04	3.81±0.01	3.60±0.07	1.52±0.03	4.53±0.07	4.95±0.15	0.46 ± 0.02	3.97±0.18	0.96±0.01	4.18±0.02
G209.00-19.38	1.78±0.01	1.63±0.05	0.72±0.02	1.94±0.32	2.03±0.08	0.47 ± 0.01	3.53±0.13	0.40±0.01	1.76±0.01
G232.62+00.99	0.93±0.01	0.88±0.07	0.38±0.03	2.30±0.05	2.90±0.21	0.49 ± 0.02	≤0.33	0.63±0.01	2.75±0.02
G211.59+01.05	0.82±0.01	0.82±0.03	0.33±0.01	1.34±0.03	1.35±0.07	0.15 ± 0.01	2.06±0.07	0.47±0.01	2.06±0.01

Notes. <sup>a</sup> The flux of H<sub>2</sub>S lines are obtained by "print area". <sup>b</sup> The beam averaged column densities of H<sub>2</sub>S are calculated by corrected optical depths. <sup>c</sup> The beam averaged column densities of H<sub>2</sub>S are derived from those of H<sub>2</sub><sup>34</sup>S with <sup>32</sup>S/<sup>34</sup>S ratios.

## Appendix C: Line widths at half maximum.

Table C.1: The line widths at half maximum in  $\text{km s}^{-1}$  for the molecules.

Source	$\text{HC}_3\text{N}$	$\text{H}_2^{34}\text{S}$	$\text{H}_2\text{CS}$	$\text{HCS}^+$	$\text{SiO}$
G000.67-00.03	$12.0 \pm 0.24$	$11.3 \pm 0.81$	$12.28 \pm 0.25$	$12.7 \pm 0.78$	$13.0 \pm 0.30$
G005.88-00.39	$5.23 \pm 0.08$	$6.38 \pm 0.14$	$4.62 \pm 0.09$	$4.86 \pm 0.24$	$27.5 \pm 0.55$
G009.62+00.19	$5.34 \pm 0.14$	$5.98 \pm 0.15$	$4.94 \pm 0.08$	$4.34 \pm 0.22$	$26.5 \pm 1.47$
G010.47+00.02	$9.64 \pm 0.06$	$6.46 \pm 0.43$	$8.37 \pm 0.06$	$7.06 \pm 0.64$	$14.9 \pm 0.56$
G010.62-00.38	$7.49 \pm 0.08$	$6.57 \pm 0.07$	$7.03 \pm 0.04$	$7.13 \pm 0.12$	$9.96 \pm 0.19$
G011.49-01.48	$1.93 \pm 0.15$	$0.66 \pm 0.39$	$2.40 \pm 0.25$	$2.50 \pm 0.51$	undetected
G011.91-00.61	$6.71 \pm 0.15$	$6.51 \pm 0.29$	$5.68 \pm 0.17$	$4.64 \pm 0.40$	$13.1 \pm 0.52$
G012.80-00.20	$5.38 \pm 0.03$	$5.57 \pm 0.12$	$5.22 \pm 0.02$	$5.38 \pm 0.07$	$7.09 \pm 0.18$
G012.88+00.48	$4.11 \pm 0.19$	$4.14 \pm 0.06$	$3.71 \pm 0.03$	$3.34 \pm 0.07$	$11.9 \pm 0.34$
G012.90-00.26	$4.77 \pm 0.10$	$4.71 \pm 0.12$	$4.51 \pm 0.08$	$4.09 \pm 0.25$	$11.8 \pm 0.55$
G014.33-00.64	$3.26 \pm 0.14$	$3.00 \pm 0.12$	$2.98 \pm 0.09$	$2.83 \pm 0.17$	$18.4 \pm 1.03$
G015.03-00.67	$2.63 \pm 0.04$	$3.85 \pm 0.32$	$2.37 \pm 0.12$	$2.25 \pm 0.29$	undetected
G016.58-00.05	$4.69 \pm 0.15$	$3.82 \pm 0.11$	$4.06 \pm 0.05$	$3.53 \pm 0.16$	$9.62 \pm 0.49$
G023.00-00.41	$6.32 \pm 0.22$	$8.14 \pm 0.34$	$4.99 \pm 0.25$	$5.71 \pm 0.62$	$17.2 \pm 0.87$
G023.44-00.18	$4.16 \pm 0.20$	$3.76 \pm 0.19$	$4.24 \pm 0.10$	$4.27 \pm 0.26$	$14.7 \pm 0.45$
G027.36-00.16	$7.46 \pm 0.19$	$6.28 \pm 0.14$	$5.43 \pm 0.06$	$4.78 \pm 0.18$	$13.0 \pm 0.33$
G028.86+00.06	$4.28 \pm 0.11$	$4.21 \pm 0.11$	$3.39 \pm 0.05$	$2.98 \pm 0.10$	$7.11 \pm 0.54$
G029.95-00.01	$6.25 \pm 0.21$	$4.67 \pm 0.09$	$3.95 \pm 0.06$	$3.69 \pm 0.20$	$10.8 \pm 0.67$
G031.28+00.06	$3.75 \pm 0.16$	$3.93 \pm 0.17$	$3.98 \pm 0.06$	$3.25 \pm 0.17$	$7.36 \pm 0.64$
G031.58+00.07	$3.36 \pm 0.11$	$3.73 \pm 0.16$	$3.39 \pm 0.06$	$3.08 \pm 0.17$	$7.09 \pm 0.28$
G032.04+00.05	$5.79 \pm 0.13$	$6.24 \pm 0.16$	$5.32 \pm 0.07$	$5.23 \pm 0.22$	$12.2 \pm 0.22$
G034.39+00.22	$2.95 \pm 0.21$	$3.29 \pm 0.32$	$3.00 \pm 0.11$	$1.86 \pm 0.14$	$4.37 \pm 0.19$
G035.02+00.34	$5.87 \pm 0.06$	$4.58 \pm 0.08$	$4.47 \pm 0.05$	$4.14 \pm 0.12$	$9.56 \pm 0.48$
G035.19-00.74	$4.73 \pm 0.07$	$5.08 \pm 0.16$	$4.58 \pm 0.06$	$3.86 \pm 0.17$	$8.63 \pm 0.44$
G035.20-01.73	$3.48 \pm 0.62$	$3.73 \pm 0.11$	$2.96 \pm 0.08$	$2.93 \pm 0.25$	$11.1 \pm 1.50$
G037.43+01.51	$2.86 \pm 0.12$	$2.63 \pm 0.14$	$2.89 \pm 0.07$	$2.65 \pm 0.19$	$4.31 \pm 0.25$
G043.16+00.01	$14.4 \pm 0.15$	$16.7 \pm 0.24$	$14.5 \pm 0.11$	$15.8 \pm 0.29$	$14.4 \pm 0.15$
G043.79-00.12	$5.94 \pm 0.17$	$5.95 \pm 0.17$	$5.48 \pm 0.06$	$5.50 \pm 0.18$	$8.78 \pm 0.25$
G049.48-00.36	$6.73 \pm 0.04$	$7.21 \pm 0.12$	$7.89 \pm 0.07$	$6.58 \pm 0.32$	$11.4 \pm 0.28$
G049.48-00.38	$9.05 \pm 0.07$	$8.46 \pm 0.09$	$7.30 \pm 0.03$	$5.89 \pm 0.12$	$10.7 \pm 0.24$
G059.78+00.06	$2.14 \pm 0.07$	$1.92 \pm 0.07$	$2.03 \pm 0.03$	$2.16 \pm 0.08$	$4.64 \pm 0.92$
G069.54+00.97	$4.20 \pm 0.06$	$3.57 \pm 0.13$	$3.39 \pm 0.06$	$3.09 \pm 0.13$	$5.56 \pm 0.29$
G075.76+00.33	$3.93 \pm 0.05$	$3.32 \pm 0.07$	$3.53 \pm 0.03$	$3.35 \pm 0.10$	$5.48 \pm 0.34$
G078.12+03.63	$4.09 \pm 0.08$	$3.96 \pm 0.32$	$4.93 \pm 0.19$	$3.64 \pm 0.37$	$29.0 \pm 1.81$
G081.75+00.59	$2.16 \pm 0.04$	$2.16 \pm 0.10$	$2.07 \pm 0.03$	$1.95 \pm 0.10$	$10.7 \pm 1.02$
G081.87+00.78	$5.49 \pm 0.05$	$4.38 \pm 0.09$	$4.43 \pm 0.04$	$4.03 \pm 0.14$	$7.73 \pm 0.14$
G092.67+03.07	$3.15 \pm 0.04$	$2.99 \pm 0.11$	$3.46 \pm 0.03$	$2.91 \pm 0.07$	$19.2 \pm 0.34$
G109.87+02.11	$4.00 \pm 0.06$	$4.60 \pm 0.17$	$3.38 \pm 0.15$	$3.14 \pm 0.32$	$14.2 \pm 0.60$
G111.54+00.77	$4.24 \pm 0.08$	$4.30 \pm 0.08$	$3.89 \pm 0.03$	$3.79 \pm 0.08$	$6.86 \pm 0.20$
G121.29+00.65	$2.60 \pm 0.04$	$2.75 \pm 0.07$	$2.59 \pm 0.03$	$2.36 \pm 0.06$	$3.79 \pm 0.20$
G123.06-06.30	$3.20 \pm 0.04$	$3.57 \pm 0.09$	$3.64 \pm 0.02$	$3.42 \pm 0.07$	$7.79 \pm 0.11$
G133.94+01.06	$4.49 \pm 0.05$	$5.28 \pm 0.09$	$3.93 \pm 0.02$	$3.81 \pm 0.05$	$6.52 \pm 0.08$
G168.06+00.82	$4.66 \pm 1.98$	$1.23 \pm 0.21$	$1.34 \pm 0.30$	$0.83 \pm 0.28$	undetected
G176.51+00.20	$1.89 \pm 0.12$	$2.98 \pm 0.33$	$2.07 \pm 0.10$	$1.60 \pm 0.23$	$14.8 \pm 1.35$
G183.72-03.66	$1.95 \pm 0.08$	$2.47 \pm 0.28$	$2.18 \pm 0.07$	$2.38 \pm 0.18$	$8.55 \pm 0.49$
G188.94+00.88	$2.49 \pm 0.17$	$3.02 \pm 0.18$	$2.63 \pm 0.05$	$2.95 \pm 0.13$	$4.00 \pm 0.24$
G192.60-00.04	$3.72 \pm 0.18$	$3.16 \pm 0.07$	$2.56 \pm 0.05$	$2.03 \pm 0.08$	$9.18 \pm 0.62$
G209.00-19.38	$2.21 \pm 0.05$	$3.13 \pm 0.11$	$2.25 \pm 0.04$	$2.35 \pm 0.11$	$18.8 \pm 0.97$
G232.62+00.99	$2.12 \pm 0.09$	$2.40 \pm 0.26$	$1.96 \pm 0.05$	$2.91 \pm 0.20$	undetected
G211.59+01.05	$3.06 \pm 0.16$	$3.27 \pm 0.12$	$3.40 \pm 0.08$	$2.58 \pm 0.28$	$6.87 \pm 0.29$

Appendix D:  $^{32}\text{S}/^{34}\text{S}$  ratios,  $\tau_{\text{H}_2\text{S}}$  and abundances.Table D.1: The information of  $^{32}\text{S}/^{34}\text{S}$  ratios,  $\tau_{\text{H}_2\text{S}}$  and abundances.

Source	$^{32}\text{S}/^{34}\text{S}$	$\tau_{\text{H}_2\text{S}}$	Abundance			
			$\text{H}_2\text{S}$ ( $10^{-9}$ )	$\text{H}_2\text{CS}$ ( $10^{-10}$ )	$\text{HCS}^+$ ( $10^{-11}$ )	$\text{SiO}$ ( $10^{-11}$ )
G000.67-00.03	16.65	6.60	$1.52 \pm 0.13$	$11.5 \pm 0.06$	$7.25 \pm 0.40$	$13.1 \pm 0.24$
G005.88-00.39	20.37	3.13	$13.9 \pm 0.26$	$24.0 \pm 0.39$	$17.8 \pm 0.68$	$56.3 \pm 0.88$
G009.62+00.19	18.91	5.77	$5.89 \pm 0.15$	$9.98 \pm 0.13$	$7.02 \pm 0.29$	$12.5 \pm 0.51$
G010.47+00.02	17.67	11.2	$15.5 \pm 0.25$	$38.3 \pm 0.23$	$35.4 \pm 1.07$	$18.2 \pm 0.44$
G010.62-00.38	19.13	5.46	$8.55 \pm 0.08$	$15.2 \pm 0.04$	$12.2 \pm 0.18$	$8.54 \pm 0.13$
G011.49-01.48	21.68	0.72	$6.37 \pm 0.25$	$10.6 \pm 0.27$	$6.70 \pm 0.44$	$14.8 \pm 0.45$
G011.91-00.61	20.22	5.21	$2.04 \pm 0.04$	$6.72 \pm 0.04$	$6.46 \pm 0.07$	$2.4 \pm 0.05$
G012.80-00.20	20.52	4.61	$4.56 \pm 0.07$	$9.39 \pm 0.07$	$6.91 \pm 0.12$	$5.43 \pm 0.12$
G012.88+00.48	20.81	10.4	$3.79 \pm 0.09$	$6.41 \pm 0.09$	$3.75 \pm 0.19$	$5.70 \pm 0.20$
G012.90-00.26	20.81	5.64	$11.8 \pm 0.59$	$37.5 \pm 0.71$	$25.0 \pm 1.24$	$51.2 \pm 2.37$
G014.33-00.64	21.76	4.39	$3.56 \pm 0.11$	$7.69 \pm 0.10$	$5.01 \pm 0.20$	$7.10 \pm 0.26$
G015.03-00.67	21.17	1.47	$2.44 \pm 0.09$	$3.25 \pm 0.08$	$2.07 \pm 0.18$	$3.99 \pm 0.16$
G016.58-00.05	20.15	5.44	$1.14 \pm 0.04$	$3.39 \pm 0.06$	$2.44 \pm 0.12$	$5.05 \pm 0.12$
G023.00-00.41	19.79	5.38	$5.78 \pm 0.10$	$16.4 \pm 0.15$	$7.82 \pm 0.24$	$18.4 \pm 0.33$
G023.44-00.18	19.20	4.49	$3.85 \pm 0.08$	$6.15 \pm 0.07$	$5.06 \pm 0.13$	$2.56 \pm 0.13$
G027.36-00.16	19.35	4.69	$10.5 \pm 0.16$	$12.6 \pm 0.16$	$8.87 \pm 0.39$	$9.86 \pm 0.44$
G028.86+00.06	19.42	5.68	$3.49 \pm 0.16$	$11.8 \pm 0.15$	$8.63 \pm 0.39$	$5.85 \pm 0.39$
G029.95-00.01	19.86	5.36	$3.39 \pm 0.16$	$8.83 \pm 0.15$	$5.03 \pm 0.24$	$6.55 \pm 0.21$
G031.28+00.06	20.30	7.96	$5.52 \pm 0.13$	$11.3 \pm 0.12$	$8.65 \pm 0.30$	$16.7 \pm 0.24$
G031.58+00.07	20.08	5.35	$1.17 \pm 0.09$	$3.15 \pm 0.09$	$1.84 \pm 0.14$	$5.34 \pm 0.17$
G032.04+00.05	20.00	5.05	$7.19 \pm 0.15$	$12.0 \pm 0.12$	$10.3 \pm 0.25$	$7.86 \pm 0.27$
G034.39+00.22	21.68	2.45	$5.89 \pm 0.26$	$15.3 \pm 0.17$	$9.98 \pm 0.37$	$6.73 \pm 0.24$
G035.02+00.34	21.25	4.56	$7.36 \pm 0.30$	$9.22 \pm 0.19$	$7.99 \pm 0.37$	$5.87 \pm 0.51$
G035.19-00.74	21.32	3.38	$2.57 \pm 0.11$	$6.80 \pm 0.14$	$5.09 \pm 0.28$	$5.64 \pm 0.25$
G035.20-01.73	20.81	3.72	$6.26 \pm 0.09$	$10.2 \pm 0.07$	$9.66 \pm 0.18$	$15.2 \pm 0.15$
G037.43+01.51	21.54	1.80	$4.40 \pm 0.16$	$10.3 \pm 0.12$	$9.22 \pm 0.26$	$8.80 \pm 0.21$
G043.16+00.01	22.05	3.31	$8.35 \pm 0.13$	$16.9 \pm 0.09$	$7.15 \pm 0.29$	$17.1 \pm 0.34$
G043.79-00.12	20.66	3.65	$11.1 \pm 0.09$	$41.5 \pm 0.17$	$19.3 \pm 0.34$	$21.4 \pm 0.52$
G049.48-00.36	21.10	3.12	$8.00 \pm 0.22$	$18.5 \pm 0.24$	$17.4 \pm 0.52$	$2.86 \pm 0.42$
G049.48-00.38	21.10	6.03	$3.07 \pm 0.15$	$6.96 \pm 0.10$	$5.16 \pm 0.20$	$6.16 \pm 0.22$
G059.78+00.06	21.98	3.66	$8.67 \pm 0.28$	$17.4 \pm 0.17$	$13.4 \pm 0.36$	$5.07 \pm 0.25$
G069.54-00.97	22.19	2.86	$5.51 \pm 0.37$	$14.3 \pm 0.44$	$10.52 \pm 0.85$	$36.0 \pm 1.62$
G075.76+00.33	22.49	1.64	$2.18 \pm 0.08$	$4.94 \pm 0.06$	$4.33 \pm 0.17$	$3.61 \pm 0.22$
G078.12+03.63	22.41	0.99	$5.90 \pm 0.11$	$15.3 \pm 0.11$	$9.01 \pm 0.26$	$20.8 \pm 0.29$
G081.75+00.59	22.49	2.46	$8.99 \pm 0.26$	$35.7 \pm 0.32$	$25.0 \pm 0.48$	$53.5 \pm 0.79$
G081.87+00.78	22.49	2.20	$3.00 \pm 0.13$	$2.94 \pm 0.06$	$2.32 \pm 0.17$	$8.32 \pm 0.27$
G092.67+03.07	22.71	2.57	$6.41 \pm 0.09$	$11.1 \pm 0.08$	$8.48 \pm 0.16$	$7.69 \pm 0.16$
G109.87+02.11	22.78	1.39	$3.71 \pm 0.16$	$10.1 \pm 0.09$	$8.64 \pm 0.18$	$6.17 \pm 0.22$
G111.54+00.77	23.51	1.72	$6.37 \pm 0.13$	$25.3 \pm 0.18$	$18.8 \pm 0.31$	$33.0 \pm 0.38$
G121.29+00.65	22.92	1.49	$10.9 \pm 0.19$	$27.7 \pm 0.17$	$21.9 \pm 0.25$	$19.2 \pm 0.21$
G123.06-06.30	23.87	2.02	$2.99 \pm 0.38$	$5.94 \pm 0.20$	$4.88 \pm 0.51$	$4.76 \pm 0.52$
G133.94+01.06	23.65	4.72	$4.37 \pm 0.36$	$13.4 \pm 0.35$	$12.4 \pm 0.78$	$24.8 \pm 1.01$
G168.06+00.82	28.11	1.06	$7.17 \pm 0.35$	$16.2 \pm 0.29$	$15.2 \pm 0.59$	$7.99 \pm 0.41$
G176.51+00.20	23.29	1.07	$8.62 \pm 0.16$	$10.9 \pm 0.18$	$11.9 \pm 0.37$	$9.50 \pm 0.44$
G183.72-03.66	23.80	1.40	$9.29 \pm 0.27$	$11.0 \pm 1.80$	$11.6 \pm 0.46$	$20.1 \pm 0.76$
G188.94+00.88	24.09	1.06	$4.00 \pm 0.14$	$6.52 \pm 0.14$	$6.6 \pm 0.35$	$9.99 \pm 0.33$
G192.60-00.04	23.73	1.62	$1.32 \pm 0.58$	$8.93 \pm 0.86$	$9.38 \pm 2.28$	$3.93 \pm 0.08$
G209.00-19.38	22.78	0.98	$5.70 \pm 0.53$	$7.22 \pm 0.25$	$6.42 \pm 0.68$	$1.27 \pm 0.01$
G232.62+00.99	23.36	0.53	$4.99 \pm 1.72$	$4.90 \pm 0.63$	$4.61 \pm 1.58$	$3.27 \pm 0.06$
G211.59+01.05	25.19	1.76	$3.20 \pm 0.25$	$8.35 \pm 0.20$	$10.5 \pm 0.78$	$1.21 \pm 0.01$

Notes. The abundance of  $\text{H}_2\text{S}$  are derived from those of  $\text{H}_2^{34}\text{S}$ .

**Appendix E: Abundance ratios.**

Table E.1: The abundance ratios between S-bearing molecules.

Source name	[H <sub>2</sub> S/H <sub>2</sub> CS]	[H <sub>2</sub> S/HCS <sup>+</sup> ]	[H <sub>2</sub> CS/HCS <sup>+</sup> ]
G000.67-00.03	1.32 ± 0.12	21.0 ± 2.18	15.9 ± 0.86
G005.88-00.39	5.80 ± 0.14	78.4 ± 3.29	13.5 ± 0.55
G009.62+00.19	5.90 ± 0.17	83.9 ± 4.06	14.2 ± 0.62
G010.47+00.02	4.06 ± 0.07	43.8 ± 1.48	10.8 ± 0.33
G010.62-00.38	5.63 ± 0.05	70.0 ± 1.20	12.4 ± 0.19
G011.49-01.48	1.48 ± 0.66	14.1 ± 7.01	9.52 ± 2.47
G011.91-00.61	6.02 ± 0.27	95.2 ± 7.20	15.8 ± 1.10
G012.80-00.20	3.03 ± 0.06	31.5 ± 0.66	10.4 ± 0.13
G012.88+00.48	4.86 ± 0.08	66.1 ± 1.51	13.6 ± 0.26
G012.90-00.26	5.91 ± 0.16	101 ± 5.68	17.1 ± 0.90
G014.33-00.64	3.15 ± 0.16	47.2 ± 3.27	15.0 ± 0.77
G015.03-00.67	7.89 ± 0.78	88.7 ± 12.5	11.2 ± 1.25
G016.58-00.05	4.63 ± 0.16	71.1 ± 3.62	15.3 ± 0.64
G023.00-00.41	7.49 ± 0.32	117 ± 11.2	15.7 ± 1.44
G023.44-00.18	3.37 ± 0.14	46.9 ± 2.90	13.9 ± 0.73
G027.36-00.16	3.53 ± 0.07	73.9 ± 2.66	20.9 ± 0.68
G028.86+00.06	6.26 ± 0.15	76.0 ± 2.51	12.1 ± 0.35
G029.95-00.01	8.28 ± 0.16	118 ± 5.46	14.2 ± 0.65
G031.28+00.06	2.97 ± 0.14	405 ± 2.62	13.6 ± 0.63
G031.58+00.07	3.84 ± 0.19	67.5 ± 4.43	17.6 ± 0.87
G032.04+00.05	4.90 ± 0.12	63.8 ± 2.63	13.0 ± 0.47
G034.39+00.22	3.72 ± 0.30	63.7 ± 6.78	17.1 ± 1.34
G035.02+00.34	6.01 ± 0.13	69.9 ± 2.21	11.6 ± 0.30
G035.19-00.74	3.84 ± 0.17	59.0 ± 3.37	15.4 ± 0.59
G035.20-01.73	7.98 ± 0.37	92.1 ± 5.72	11.6 ± 0.59
G037.43+01.51	3.79 ± 0.18	50.6 ± 3.51	13.4 ± 0.78
G043.16+00.01	6.14 ± 0.10	64.9 ± 1.53	10.6 ± 0.21
G043.79-00.12	4.27 ± 0.16	47.7 ± 2.14	11.2 ± 0.33
G049.48-00.36	4.94 ± 0.07	117 ± 5.00	23.6 ± 0.96
G049.48-00.38	2.66 ± 0.02	57.1 ± 1.07	21.5 ± 0.37
G059.78+00.06	4.33 ± 0.13	46.0 ± 1.84	10.6 ± 0.34
G069.54-00.97	4.41 ± 0.22	59.5 ± 3.68	13.5 ± 0.55
G075.76+00.33	4.98 ± 0.16	64.5 ± 2.64	12.9 ± 0.35
G078.12+03.63	3.85 ± 0.28	52.4 ± 5.50	13.6 ± 1.17
G081.75+00.59	4.41 ± 0.17	50.3 ± 2.67	11.4 ± 0.47
G081.87+00.78	3.85 ± 0.07	65.5 ± 2.23	17.0 ± 0.51
G092.67+03.07	2.52 ± 0.07	36.0 ± 1.21	14.3 ± 0.28
G109.87+02.11	10.2 ± 0.49	130 ± 11.1	12.7 ± 0.97
G111.54+00.77	5.80 ± 0.09	75.6 ± 1.76	13.0 ± 0.26
G121.29+00.65	3.67 ± 0.16	43.0 ± 2.01	11.7 ± 0.27
G123.06-06.30	2.52 ± 0.05	33.9 ± 0.85	13.5 ± 0.22
G133.94+01.06	3.94 ± 0.07	49.8 ± 1.00	12.6 ± 0.15
G168.06+00.82	10.2 ± 3.74	108 ± 52.6	10.6 ± 3.88
G176.51+00.20	5.03 ± 0.67	61.3 ± 10.1	12.2 ± 1.34
G183.72-03.66	3.27 ± 0.28	35.2 ± 3.63	10.8 ± 0.72
G188.94+00.88	4.41 ± 0.22	47.1 ± 2.87	10.7 ± 0.44
G192.60-00.04	7.94 ± 0.19	72.8 ± 2.61	9.16 ± 0.32
G209.00-19.38	8.44 ± 1.40	80.4 ± 3.87	9.53 ± 1.60
G232.62+00.99	3.83 ± 0.31	30.4 ± 3.27	7.94 ± 0.61
G211.59+01.05	6.14 ± 0.25	61.1 ± 3.87	9.95 ± 0.58